PROBABILISTIC CORTICAL AND MYOCARDIAL FIBER TRACKING IN DIFFUSION TENSOR IMAGING

by

Rakesh M. Lal

A thesis submitted to The Johns Hopkins University in conformity with the requirements for the degree of Master of Science in Engineering

Baltimore, Maryland
July, 2001

Abstract

This thesis involves the tracking of white matter and heart fibers, using diffusion tensor imaging data and high resolution MR scans. Dynamic programming is employed to generate fibers linking regions of interest in the brain and heart with paths that minimize an energy constraint.

From the diffusion tensor data it is possible to determine the probability that a fiber passing through a particular voxel is oriented in a particular direction. One can define the energy associated with a path connecting a given voxel to one of its neighboring voxels as the inverse of the probability of a fiber being oriented in the direction of this neighbor. In addition assume this energy is additive. Thus the energy associated with a path between two voxels and passing through a third voxel, is the equal to the sum of the energies associated with the path from the starting voxel to the intermediate voxel and the path from the intermediate voxel to the ending voxel. Thus to determine the optimal path between a start and an end voxel, we search over all paths connecting the two voxels and choose the path in which the total energy is minimized. In order for this search to be performed more efficiently, dynamic programming is used to reduce the complexity of the problem.

In addition a technique to extend the dynamic programming algorithm is presented to take into account not only the diffusion tensor information, but also accomodate any prior information about the Frenet characteristics of cortical and myocardial fibers. Properties of average curvature and average torsion of the fibers are incorporated into the cost function of the dynamic programming algorithm, so as to better model fibers.

Acknowledgements

I would like to express my deepest gratitude to my advisor, Dr. Michael I. Miller for all his support and guidance during this project and for the exciting and challenging environment he has provided for us. His enthusiasm and confidence in me has been a tremendous source of inspiration. I am also indebted to my undergraduate advisor, Dr. Murray B. Sachs who has always shown a vested interest in my success, and provided my with sound advice whenever I needed it.

Special thanks to Dr. Susumu Mori and Dr. Xavier Golay, who were instrumental in providing me with high quality data, and were always willing to share their knowledge and expertise. I would also like to thank Allan Massie who assisted me in the development and optimization of the algorithm. Also, I must thank Dr. Tilak Ratnanather for his interest, guidance and advice in completing this project.

I would also like to thank my fellow student in the Center for Imaging Science with whom I have been priviledged to work, for all the encouragement and discussion we shared. I must thank those senior to me, particularly Faisal Beg, Cash Costello, and Paritosh Tyagi for all their advice. In addition, Dmitri Bitouk, Marc Vaillant, Guang-Lih Huang, and Srinivas Peddi have always provided a stimulating and intellectually rich environment. I also appreciate all the friendships I formed at the center, with Jeff Homer, Raymond Hulse, Aashish Majethia, Agatha Lee, Walter Barmak, Dawn Kilheffer, and Pam Lauria.

Finally, I would like to thank my parents and family for all their affection, encouragement and motivation to further my education. They have always shown a tremendous amount of faith in me, and gave me the support and motivation I needed, and for this I am eternally grateful.

Rakesh Lal

Table of Contents

List of Tables

List of Figures

Chapter 1

Introduction

1.1 Computational Anatomy

The discipline of computational anatomy can be seen as the application of scientific, mathematical, and computational tools to the study of anatomy and its variability. It has been described by Grenander and Miller [12] as an aspect of geometry that is influenced by pattern theoretic principles, and whose kinematics is described in terms of concepts borrowed from continuum mechanics. In particular, they discuss that the main object of study in computational anatomy is biological variability, and the ability to characterize biological variance permits the generation of typical anatomical structures from a template, through the application of diffeomorphic transformations.

In order to motivate the application of techniques of computational anatomy, it is necessary to describe the cortical surface study methods developed by our group at the Center for Imaging Science, Johns Hopkins University. Automated methods for the segmentation of white matter and gray matter from MR images using parameter estimation from the EM algorithm [23] have been implemented, as have cortical surface generation through isosurfaces. Algorithms for tracking 1-D submainfolds, namely sulcal, gyral and geodesic curves on the cortical surface, using dynamic programming have also been developed [13]. Other ideas involving the matching of these curves via Frenet distances have also been developed and implemented [15].

Based on the foundation built by these methods, it is possible to develop computational techniques and algorithms to quantify and solve the problems associated with tracking white matter neuronal projections and heart myofibers. In a fashion similar to

the algorithm developed for the tracking of geodesics on the cortical surface, dynamic programming can be applied to diffusion tensor imaging data to compute optimal curved paths through a volume. Concepts derived from matching curves using Frenet distances can also be used to incorporate prior information of the Frenet properties of fibers into the dynamic programming algorithm, thus allowing for a more realistic reconstruction of fibers. The next section further discusses the problem of fiber tracking, and how concepts from the field of computational anatomy, engendered by Dr. Ulf Grenander and later championed by Dr. Michael Miller, can be used to solve these problems.

1.2 Tracking Fiber Projections

The study of white matter tracts in the human brain plays a critical role in elucidating brain anatomy, functionality and pathology. Currently, there are two major approaches to understanding the organization of the nervous system in the brain. One method involves the mapping of functional domains onto anatomical images, and techniques such as positron emission tomography (PET) and functional MRI (fMRI) have provided insight into the local functional specialization of the brain, particularly for tasks such as cognition [30]. Unfortunately, this approach provides little data on the anatomical fiber connections linking different regions of the brain, and understanding the anatomical structure relies primarily on invasive in vivo techniques in postmortem tissue [29], [28], and [30].

Electrical propogation and force generation in the heart is also dependent on the orientation and organization of myocardial fibers [7]. It is known that the spread of current occurs maximally in the direction of the long axis of the fiber, and as a result, abnormalities in the myocardial architecture are indicative of diseased states of the heart such as arrhythmias [32], [33]. Hence characterization of the microstructure of both diseased and normal hearts provide insight into the cardiac electromechanics of hearts in both normal and diseased states. Similar to white matter neuronal projections, reconstruction of myocardial fibers is based on invasive histological techniques. The process is quite intensive and in standard techniques, tissue must be specially prepared which may itself alter the myocardial structure [33].

As a result, there is a great need for a reconstruction algorithm that is both non-invasive and can be performed in a reasonable amount of time. Through the use of diffusion tensor imaging, it is possible to reconstruct 3 dimensional models of both white matter

tracts and myocardial fibers by tracking the fiber path that minimize an energy function that is based on the diffusion tensor data. The principle behind diffusion tensor imaging is that in the brain and heart, the directionality of water diffusion is anisotropic [26], [27], [33]. Specifically in the brain and heart, water preferentially diffuses parallel to fiber bundles. From the diffusion tensor data, it is possible to obtain not only a 3 dimensional reconstruction of fibers, but also a unique contrast called an anisotropy map, that is believed to reflect fiber density [27]. In diffusion tensor imaging, a 3×3 matrix is obtained, and the eigenvectors and eigenvalues of this matrix define an ellipsoid that describes the diffusive characteristics of water at each voxel in the image. Fiber reconstruction algorithms that track the path generated by thresholding the direction of maximal diffusion currently exist, but these algorithms are quite sensitive to noise [13].

In this thesis, a different approach to track the optimal curve trajectories through a volume, based on dynamic programming, is proposed. The tracking problem is posed as an optimization problem and instead of locally thresholding the direction of highest diffusivity of water, a path between chosen start and end points, that globally minimizes a sequentially additive energy constraint defined by the diffusion tensor imaging data is computed. If $D(x)$ is the 3×3 diffusion tensor matrix for a voxel x, then define the energy associated with a unit path from voxel x in a direction v as $v^T D^{-1}(x) v$. To reduce the time complexity dynamic programming [1] is used to perform the search. Using this algorithm, various white matter and myocardial fibers were tracked. White matter reconstructions were performed on the commissural fibers of the corpus callosum, fibers in the internal capsule, and the visual pathways from the lateral geniculate nucleus (LGN), to the calcarine sulcus. In the heart, fibers running from the epicardium to the endocardium of the free wall of the left ventricle were reconstructed. In order to incorporate prior information of such fibers we construct a statistical model based on the Frenet representation of curves [15], and include mean curvature and torsion into the energy function [13]. Currently, these variables are left as parameters passed to the algorithm, but it is possible to estimate them give accurate anatomical data [13].

1.3 Thesis Layout

Chapter 2 describes in detail the methods and algorithms used in the study. First, it details the manner in which diffusion tensor MR scans are carried out. It begins with a brief

overview of the workings of an MR scanner, and describes different types of MR images. Subsequently, it explains the physics behind the acquisition of diffusion tensor imaging. Next, the dynamic programming algorithm is presented in detail. The general algorithm as described by Bertsekas in [1] is outlined, and then the algorithm is tailored to solve the tracking problem defined in the earlier section. In particular, the sequentially additive cost function used in the dynamic programming algorithm is described. Extensions to the basic algorithm to accomplish tracking the optimal K paths linking regions is also presented.

Chapters 3 presents results of the implemented algorithm described in chapter 2 on both real and synthetic data sets. The first half of chapter 3 primarily deals with results obtained from running the algorithm on phantom data sets, in order to validate the accuracy of the implementation. The subsequent half presents result of the algorithm on brain and heart data sets obtained from the labs of Dr. Peter van Zijl and Dr. Raymond Winslow respectively. Various classical cortical and myocardial fiber pathways were reconstructed, and shown. Fiber paths in the brain generated through dynamic programming, and through principal eigenvalue thresholding is are also compared in this chapter.

Chapter 4 describes a more mathematically formal method of describing the curves generated from the tracking algorithm by using Frenet distances. It begins by describing the Frenet representation of curves, and describes how this model was used to incorporate prior information about the curvature and torsion of fibers into the algorithm.

Chapter 2

Methods and Algorithm

2.1 Diffusion Tensor Analysis

2.1.1 Conventional MRI

In order to understand difusion tensor imaging, it is important to have a basic knowledge of the principles of conventional magnetic resonance imaging. Magnetic resonance imaging is based, on the principle that the application of a magnetic field on a body causes the water protons to align themselves parallel to the magnetic field. The magnetic field generated as a result of the spin of the protons is called the net magentization. In the equilibrium state, the net magnetization only has a component in the direction of the external magnetic field. Conventionally this is labelled as the z-component, M_z. The component of the magnetization vector lying in the plane normal to M_z is called the transverse magnetization, M_{xy}.

By applying a radio wave at a resonant frequency it is possible to place the net magnetization orthogonal to the applied magnetic field, such that $M_z = 0$. This results in the magnetization vector precessing about the axis of the applied magnetic field at the frequency of the RF pulse. This frequency is known as the Larmor frequency, and is dependent on the strength of the external magnetic field and the specific atom.

$$\nu = \gamma B \tag{2.1}$$

where γ is the gyromagnetic ratio of the particle and B is the magnetic field strength. For hydrogen, $\gamma = 42.58$ MHz / T.

After the external radio frequency pulse is applied, the system returns to equilibrium as the xy component of the magnetization, M_{xy} decays, and the z component M_z recovers. This combined process is known as relaxation, and is governed by the following equations.

$$M_z = M_0(1 - e^{-t/T_1}) \tag{2.2}$$

$$M_{xy} = M_{xy_o} e^{-t/T_2} \tag{2.3}$$

where M_0 is the equilibrium z component of the net magnetization, and M_{xy_o} is the initial transverse magnetization after the RF pulse has been applied.

2.1.2 Frequency Encoding and Slice Selection

When in a uniform magnetic field, protons precess with a constant Larmor frequency. However, if instead a gradient field is applied, the Larmor frequency of the protons now depends on the position of the protons in the material. This procedure is known as *Frequency Encoding.*

Slice selection is achieved using frequency encoding. During the application of the RF pulse necessary to rotate the spins of the protons, a gradient magnetic field is applied in the direction of the external magnetic field. Now the Larmor frequency of each spin is dependent on its z coordinate. Hence a particular RF pulse excites protons located in a single slice of the object being imaged.

2.1.3 Phase Encoding and Fourier Transform Tomography

The process of *Phase Encoding* involves the application of a gradient magnetic pulse to impart a specific phase angle to the transverse magnetization. By applying a gradient in a particular direction, the protons precess with a Larmor frequency dependent on the position of the protons in the material. If this magnetic field gradient is then turned off, the protons once again begin to precess at a constant frequency, independent of position. However, their precessions are now out of phase with each other with the phase difference being determined by the magnitude and duration of the phase encoding gradient pulse.

In Fourier Transform Tomography imaging, the phase encoding gradient pulse is usually applied after the slice has been selected, and is applied in a direction perpendicular

to the slice selection gradient. Once the phase encoding gradient is removed, the protons in the slice being imaged precess at a constant frequency, but are out of phase. Subsequently, a frequency encoding pulse is applied in the direction perpendicular to both the slice selection and phase encoding gradients and the resulting free induction decay (FID) is measured. The process from the application of the phase encoding pulse is repeated with phase encoding gradients of varying magnitudes, and a two dimensional signal is obtained. Fig. 2.1 illustrates the gradient pulses applied to obtain the FID. Taking the two dimensional Fourier Transform of this signal results in the MR image.

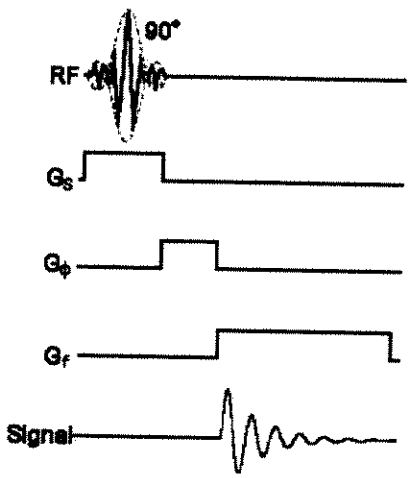

Figure 2.1: A timing diagram showing the pulse sequence for an FID using FT tomography. G_s is the slice selection gradient, G_ϕ is the phase encoding gradient, and G_f is the frequency encoding gradient.

2.1.4 T_2 Weighed Imaging

T_2 weighted imaging is an example of a protocol that generates a relaxation weighted image. It relies on measuring the rate of decay of the transverse component of the magnetization vector. After the RF pulse is applied to excite the protons, the transverse component of the magnetization vector gradually decays as the precession of the protons become more randomized. Since the signal measured is the vector sum of the individual magnetization vectors of the spin of the protons, the dephasing of these vectors leads to a loss of signal. By measuring the reduction in the SNR of the signal, it is possible to determine the time constant of the T_2 relaxation. It is thought that when water protons are in a region of low

viscousity, the T_2 relaxation time is slower. The more molecular interractions the faster the decay.

In a standard MR image, the quantity being measured is the proton density of the body. In a T_2 weighted image, this quantity is weighted by the T_2 relaxation properties of the different regions in the body. The adantage of a T_2 weighted image is that the proton density conveys little information about the type of tissue, and has low contrast if the water molecules are relatively evenly distributed. The T_2 weighted image adds contrast based on the tissue types of the body being imaged. Such an image is obtained by introducing a time period between the excitaiton phase and the acquisition phase. This period is called the echo time (TE) and the larger the TE, the heavier the T_2 weighting. See Fig. 2.2 for examples of proton density images and T_2 weighted images.

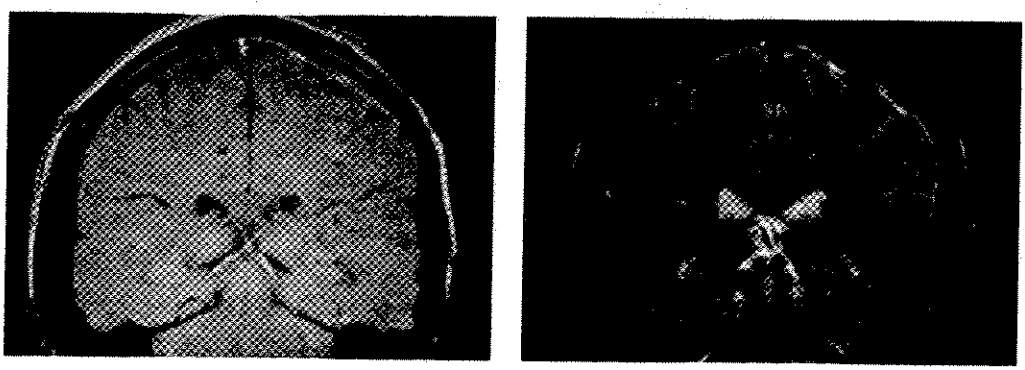

(a) (b)

Figure 2.2: Examples of different types of MR images. (a) Proton density image. (b) T_2 weighted MR image.

2.1.5 Diffusion Tensor Imaging

In diffusion tensor imaging, a set of coefficients are obtained by sensitizing the magnetic resonance (MR) signal to random motions by applying strong magnetic field gradient pulses [30]. In an MR scan, if the magnetic field is kept homogeneous, the precession rate of the protons is also homogeneous. By applying a magnetic field gradient, the precession of the protons become out of phase with each other, depending on the direction of the field gradient. If a subsequent field gradient pulse of identical direction and duration, but opposite magnitude to the first is applied, the precession of the protons should become refocused or re-phased. This phenomenon is illustrated in Fig. 2.3. However, if the protons

moved in between the application of these two gradient pulses, the refocusing cannot be perfect. Thus by applying a pair of gradient pulses with a known time interval between them, the MR signal can be made sensitive to motional processes such as flow or diffusion [26].

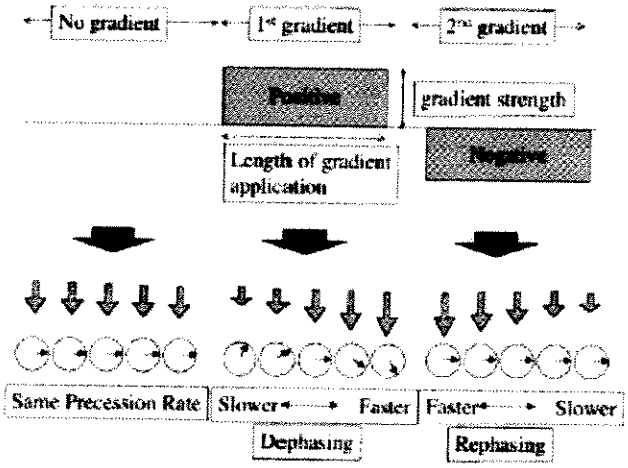

Figure 2.3: A dephasing gradient is first applied causing non-uniform precession frequencies. Subsequently a rephasing gradient is applied, causing a restoration in phase and precession frequency. This rephasing is complete only if there is no random motion of the particles due to motional processes.

The diffusion coefficients can be determined by measuring the amount of signal loss due to the gradient pulse intensity and direction. This signal intensity reduction is given by

$$ln(S/S_0) = -\gamma^2\delta^2 t_{dif} \sum_{i,j} G_i D_{ij} G_j \tag{2.4}$$

where γ is the gyromagnetic ratio of protons, δ is the gradient length, t_{dif} is the time between application of the gradient pulses, and G is the intensity of the gradient pulse. By varying the gradient directions, the diffusion coefficients along six independent axes can be measured to determine the symmetric diffusion tensor [27]

$$D = \begin{bmatrix} D_{xx} & D_{xy} & D_{xz} \\ D_{xy} & D_{yy} & D_{yz} \\ D_{xz} & D_{yz} & D_{zz} \end{bmatrix} \tag{2.5}$$

From this tensor we can derive an ellipsoid associated with each voxel that is defined by the eigenvalues and eigenvectors of the diffusion tensor matrix [26]. Once we completely define the ellipsoid it is possible to then use fiber tracking algorithms to trace various fiber paths. There is evidence to suggest that brain water diffuses parallel to bundles of axons rather than perpendicular to them [28]. Thus traking the dominant path of the diffusion of water in the brain allows for the reconstruction of neuronal projections [30]. Evidence suggests that myocardial heart fibers can also be reconstructed in a similar manner [32]. In this paper, we outline the use of dynamic programming [1] to optimally track white matter fibers and myocardial heart fibers.

2.2 Dynamic Programming

2.2.1 Basic Problem

Dynamic programming is a very useful tool that reduces the complexity of the search for a globally optimal solution on a graph. Its application varies from solving routing problems in computer networking, to use in speech recognition. Dijkstra's algorithm in networking, and Viterbi's algorithm in speech processing are both instances of dynamic programming.

The basic problem that dynamic programming tries to solve is as follows. Consider a discrete time dynamic system of the form

$$x_k = f\left(x_{k-1}, u_{k-1}(x_{k-1}), w_{k-1}\right) \tag{2.6}$$

where x_k is a state variable, u_k is a control or decision variable, and w_k is random noise, with a sequentially additive cost function $g_k\left(x_k, u_k(x_k), w_k\right)$ incurred at each time k, such that the total cost along a sample trajectory is given by

$$g_N\left(x_N\right) + \sum_{k=0}^{N-1} g_k\left(x_k, u_k(x_k), w_k\right) \tag{2.7}$$

determine the set of controls $\{\ u_0, u_1, \cdots, u_{N-1}\ \}$ that minimizes the expected cost

$$E\left[g_N\left(x_N\right)+\sum_{k=0}^{N-1} g_k\left(x_k, u_k(x_k), w_k\right)\right] \tag{2.8}$$

The dynamic programming concept relies on the *principle of optimality.* This means that if $\pi^* = \{ \mu_0^*, \mu_1^*, \cdots, \mu_{N-1}^* \}$ is an optimal control law for the basic problem with $k = 0 \cdots N$, then the truncated control law $\{ \mu_i^*, \mu_{i+1}^*, \cdots, \mu_{N-1}^* \}$ is an optimal control law for the subproblem of minimizing the cost function

$$E\left[g_N\left(x_N\right)+\sum_{k=i}^{N-1} g_k\left(x_k, u_k(x_k), w_k\right)\right] \tag{2.9}$$

with $k = i \cdots N$.

In the following section, the dynamic programming algorithm and its application to tracking neuronal projections using diffusion tensor data is discussed further. This problem is a simplification of the basic problem defined above, as the random noise w_k is assumed to be zero. In this case the problem reduces to determining the optimal control law $\{ u_0, u_1, \cdots, u_{N-1} \}$ that minimizes the cost (which is equal to the expected cost)

$$g_N\left(x_N\right)+\sum_{k=i}^{N-1} g_k\left(x_k, u_k(x_k), w_k\right) \tag{2.10}$$

2.2.2 Tracking Algorithm

Each voxel in the volume has a symmetric 3×3 diffusion tensor ($\mathbf{D}$) and corresponding eigenelements $(\lambda_i, \phi_i)_{i=1,2,3}$ associated with it. These characterize the diffusive properties of water at the voxel. In particular the eigenvector associated with the largest eigenvalue corresponds to the direction of fastest diffusion. Tracking algorithms that employ principal eigenvalue thresholding currently exist [27], [28], [29], [30].

In order to apply dynamic programming to the problem of tracking optimal curved trajectories through a volume [13], a fundamentally different approach must be taken. Define the center point of each voxel in the volume to be a node and associate a sequentially additive energy function with arcs linking neighboring nodes. The problem then reduces to computing the minimum energy path linking start and end nodes.

Let S be the finite state space of size $||S|| = N$ and define $c^k(i, j)$ as the cost of the transition from $i \in S$ to $j \in S$ at time k. If the cost is additive over the length of the path, and we assume that the optimal path between two points passes through no more

than K nodes, then dynamic programming reduces the complexity of the search to order of KN^2. In applying dynamic programming, we define the state space S_k as the the subset of nodes that can be reached from the initial node in k steps with a finite cost. In addition, assume that $c^k(i,j) \geq 0$, and that $c^k(i,j) = \infty$ implies that no transition from node i to node j exits. Also, note that the optimal path cannot pass through more than N nodes, so we set $K = N$. Furthermore, we permit the degenerate move from a node i to itself with cost $c^k(i,i) = 0, \forall i$. This degenerate move allows paths with length less than N to be considered.

Definition 1 *Given the starting node x_0, define node x_i as $x_i = x_0 + \sum_{j=0}^{i-1} v_j$ where v_j is a unit vector in R^3. Define $\mathcal{P}_N(x_0, x_N)$ to be all N-length paths starting at node x_0 and ending at node x_N. A path $\pi(x_0, x_N) \in \mathcal{P}_N(x_0, x_N)$ with cost $J(\pi(x_0, x_N))$ is the sequence of nodes $\pi(x_0, x_N) = \{x_0, x_1, \ldots, x_N\}$, with cost $J(\pi(x_0, x_N)) = \sum_{i=0}^{N-1} c^i(x_i, x_{i+1})$. The optimal N-length path is given by*

$$\pi^*(x_0, x_N) = \underset{\pi \in \mathcal{P}_N(x_0, x_N)}{\arg\min} \sum_{i=0}^{N-1} c^i(x_i, x_{i+1}) \tag{2.11}$$

Theorem 1 *The optimal N-length path cost from node s to node t, $J(\pi^*(s,t))$ is given by $J(\pi^*(s,t)) = J_0(s,t)$, where J_0 is given by the final step of the following algorithm, with $J_{N-1}(i,t) = c^{N-1}(i,t)$, and*

$$J_k(i,t) = \min_{j \in S} \{c^k(i,j) + J_{k+1}(j,t)\},$$

where $k = 0, 1, \ldots, N-2, i \in S$ and $J_0(i,t)$ evaluated at $i = s$.

Proof *The proof is to show that $J_k(i,t)$ is the optimal path cost from node $i \in S$ to $t \in S$ in $(N-k)$ moves. Then $J_0(s,t)$ is the case where $k = 0$ evaluated at $i = s$. We prove this by induction on k. $J_{N-1}(i,t)$ is clearly the optimal path cost in one move, since there can be at most one path of length 1 between two nodes. Now suppose that $J_n(i,t)$ is the optimal $(N-n)$ length path cost between nodes i and t. The optimal $(N-n+1)$ path cost from node i to node t must be given by $J_{n-1}(i,t) = \min_{j \in S} \{c^k(i,j) + J_n(j,t)\}$. Hence the theorem holds for $k = N-1, N-2, \ldots, 0$.*

Fig. 2.4 illustrates the application of the dynamic programming algorithm to the problem of recognizing road surfaces from aerial images [11]. Define each pixel in the

dataset to be a node, and set the cost of a transition from one pixel to another in the 8-neighborhood space to be $(I - I_\mu)^2/\sigma^2$, where I is the intensity of the pixel, I_μ is the mean intensity of a road surface and σ^2 is the variance in the intensity of road surfaces in the data set. Dynamic programming can then be employed to calculate the lowest energy path as shown in Fig. 2.4(b), where 3 pairs of start and end seed points labelled A-F were selected. The paths determined by the algorithm travel along low intensity pixels in the images as these correspond to road surfaces due to the appropriate choice of I_μ and σ. The histogram in Fig. 2.4(c) shows the drastic difference in path cost between the optimal path and 10000 other randomly generated paths between points C and D.

(a) (b)

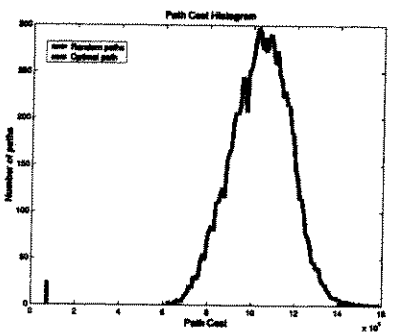

(c)

Figure 2.4: Application of dynamic programming to track road surfaces. (a) An aeiral view of San Francisco International Airport. (b) Three road surface paths generated using dynamic programming. (c) Histogram showing the computed cost of 10000 randomly generated paths between two points. The red line indicates the cost of the optimal path, which is significantly lower than that of the random paths.

2.2.3 Probabilistic Labelling of Paths

The application of dynamic programming to the tracking of fiber tracts in diffusion tensor imaging is presented in this section. The center of each voxel in the volume is defined as a node and the state space S is the collection of these nodes. A voxel j is in the neighborhood of voxel i if j is immediately adjacent to i in the 26-connected sense. There is a direct transition from node x_i to node x_j, representing the centers of voxels i and j respectively, if and only if j is in the neighborhood of i.

Definition 2 *Define the probability associated with a transition between connected nodes x_i and x_{i+1} to have a Gaussian distribution with covariance matrix $D(x_i)$. Then the probability of an N-length path $\pi_N(x_0, x_N)$ is given by the product of the quadratic form of the individual direction vectors v_i between subsequent nodes along the path as*

$$P\left[\pi_N(x_0, x_N)\right] = \prod_{i=0}^{N-1} \frac{e^{-\frac{1}{2}\left[v_i^T D(x_i)^{-1} v_i\right]}}{(2\pi)^{3/2}[det(D(x_i))]^{1/2}} \tag{2.12}$$

Proposition 1 *The maximum probability N-length path $\pi^*(x_0, x_N)$ is given by*

$$\pi^*(x_0, x_N) = \underset{\pi \in \mathcal{P}_N(x_0, x_N)}{\arg\min} \sum_{i=0}^{N-1} \left\{ v_i^T D(x_i)^{-1} v_i + ln(\lambda_1(x_i)) + ln(\lambda_2(x_i)) + ln(\lambda_3(x_i)) \right\} \tag{2.13}$$

Proof *From the probability of an N-length path (Eq. 2.12) the maximum probability path is given by*

$$\pi^*(x_0, x_N) = \underset{\pi \in \mathcal{P}_N(x_0, x_N)}{\arg\max} \prod_{i=0}^{N-1} \frac{e^{-\frac{1}{2}\left[v_i^T D(x_i)^{-1} v_i\right]}}{(2\pi)^{3/2}[det(D(x_i))]^{1/2}} \tag{2.14}$$

By taking the natural log of the equation for the maximum probability path (Eq. 2.14), and using the fact that $det(D(x_i)) = \lambda_1(x_i)\lambda_2(x_i)\lambda_3(x_i)$, we obtain the desired result (Eq. 2.13).

Note that this is a sequentiallly additive cost function and hence it is possible to use dynamic programming to compute the optimal path and its associated cost. The path $\pi^* = \{x_0, x_1, \ldots, x_N\}$ that minimizes this function is the optimal path.

As defined in Theorem 1, it is possible to compute the optimal path by searching over the entire state space S at step k. However, it is possible to apply dynamic programming to reduce the complexity by examining restricted state spaces $S_k \subset S$, and iteratively computing the optimal $N-k$ length paths, for $k = N-1, N-2, \ldots, 0$.

Proposition 2 *For any node $x \in S_k$, denote P_x as the set of nodes $\{n\}$ such that a direct transition from x to n exists. Define the cost $c^k(x_i, x_j) = v_i^T D^{-1}(x_i) v_i + ln(\lambda_1(x_i)) + ln(\lambda_2(x_i)) + ln(\lambda_3(x_i))$ for $x_j \in P_{x_i}$, and $c^k(x_i, x_j) = \infty$ for $x_j \notin P_{x_i}$. The optimal N-length cost $J_0(s)$ from s to t is given by the final step of the following algorithm evaluated at $i = s$.*

Algorithm 1 *Initialize: $J_k(i) = \infty \quad i \neq t$, $J_k(t) = 0$ for all k; $S_N = \{t\}$;*
For every $k = N - 1$ to 0,

$$S_k = \{i | i \in P_j, j \in S_{k+1}\}; \text{ set } c^k(i,j),\ i \in S_k \text{ and } j \in S_{k+1}.$$
$$J_k(i) = \min_{j \in \{S_{k+1} \cap P_i\}} \{c^k(i,j) + J_{k+1}(j)\}, i \in S_k$$

end

Proof *The proof is by induction on k. The inductive hypothesis is that $J_k(i)$ is the minimum cost from node i to node t in $(N - k)$ steps, for all $i \in S_k$. For the initial case $k = N$ this hypothesis is clearly true. Assume it is true for some $k = n$, and now consider $k = n - 1$. Suppose for the sake of contradiction, an optimal path π^* of length $(N - n + 1)$ from node $i \in S_{k+1}$ to node t with cost $J^* < J_{n-1}(i)$ exists. Since the path is optimal, then the subpath of length (N-n) starting from node $j \in P(i)$ where j is the second node along the path π^*, and ending in node t must also be optimal. From the inductive hypothesis, its cost must be $J_n(j)$, and since $j \in P(i)$, we get that $J^* \geq J_{n-1}(i)$, which is a contradiction. Hence the induction is complete.*

Note that the optimal path $\pi_k(i)$ associated with $J_k(i)$ is given recursively by

$$\pi_N(i) = \{t\}$$
$$\pi_k(i) = \pi_{k+1}(i) \cup \{j\}, \text{ where } j \text{ minimizes } J_k$$

2.2.4 Comparison of DP with other Search Algorithms

In determining the utility of an algorithm it is important to compare the complexity of the algorithm with other algorithms that can be implemented to solve the problem. Complexity is characterized by both the runtime of the algorithm on increasingly larger data sets, as well as the space requirements of the algorithm. Other criteria to judge the utility of a search algorithm are whether the solution found is guaranteed to be optimal, and whether the search is complete.

Algorithm	Time	Space	Optimal	Complete
Breadth-First	b^d	b^d	Yes	Yes
Uniform-Cost	b^d	b^d	Yes	Yes
Depth-First	b^m	bm	No	No
Iterative-Deepening	b^d	bd	Yes	Yes
Bidirectional	$b^{d/2}$	$b^{d/2}$	Yes	Yes
Dynamic Programming	bmn	n	Yes	Yes

Table 2.1: Evaluation of various search strategies. b is the branching factor; d is the depth of the optimal solution; m is the maximum depth of the search tree; n is the number of nodes at each depth of the tree.

The search problem to be solved in tracking neuronal projections using diffusion tensor imaging involves finding the optimal path between start and end points over a deterministic search tree. There are numerous strategies that can be employed to solve this problem. These include a Breadth-First search, a Uniform-Cost search, a Depth-First search, an Iterative Deepening search, and a Bidirectional search. For a rigorous treatment of each of these strategies, see [8]. Table 2.1 compares these search strategies along with the dynamic programming algorithm in terms of the criteria of time complexity, space complexity, optimality of solution, and completeness of the search.

2.3 Extensions to the basic algorithm

2.3.1 Region to Region Tracking

It is difficult to discern neuronal connectivity in a highly structured organ such as the brain given optimal paths from a single voxel to another voxel. A better tool to elucidate neuronal anatomy would be the computation of top k optimal trajectories linking a starting set or region of voxels to another ending region of voxels. This problem consists of two sub-problems. The first is to extend the dynamic program algorithm to compute the optimal path linking two regions, instead of linking two nodes. The second sub-problem is to compute the best k paths linking these regions as opposed to the optimal. This section illustrates a simple solution to the first sub-problem, and the second is addressed in the subsequent section.

It is possible to reduce the problem of computing the optimal path between regions to one of computing the optimal path between two nodes in the state space by altering the state space. Once this is done, dynamic programming can then be applied to solve the problem. The modification of the state space is as follows. Given a starting set of nodes $\mathcal{S}$ and an ending set of nodes $\mathcal{T}$, introduce two "dummy nodes" s and t into the state space, such that there is a transition from s to every node in $\mathcal{S}$ in the first time step with cost 0, and there is a transition from every node in $\mathcal{T}$ to node t with cost 0, at all time steps. Hence $c^0(s,n) = 0, \forall n \in \mathcal{S}$, and $c^k(n,t) = 0, \forall n \in \mathcal{T}, \forall k$.

Proposition 3 *The path formed by removing the first and last arcs from the optimal path between nodes s and t is the optimal path between the sets of nodes $\mathcal{S}$ and $\mathcal{T}$.*

Proof *Let π^* be the optimal path between dummy nodes s and t, and let π_0^* be the optimal path between the sets of nodes $\mathcal{S}$ and $\mathcal{T}$. Suppose for the sake of contradiction that π_0^* is not the path formed by removing the first and last arcs of π^*. Consider the path formed by prepending the arc between s and the starting node of π_0^* and appending the arc between the ending node of π_0^* and t. The cost of this path is less than π^*, since π_0^* is the best path between the sets $\mathcal{S}$ and $\mathcal{T}$, and the costs of the transitions from s to any node in $\mathcal{S}$ and from any node in $\mathcal{T}$ to t are 0. However this is a contradiction since π^* is the optimal path between s an t, and hence the proposition is true.*

From Proposition 3 it is clear that the introduction of the "dummy nodes" into the state space, does infact lead to the computation of the optimal path between a starting set of nodes and an ending set of nodes.

2.3.2 Shortest K-Paths Problem

Apart from computing the optimal path from a starting set of nodes to an ending set of nodes, the determination of the best k paths (as opposed to a single path) can also provide useful insight into the connectivity of the brain, especially regarding fiber bundles. This section presents another extension to the dynamic programming algorithm to compute the optimal k paths between two sets of nodes, described in [19] and [20].

The first step in this algorithm is to determine the shortest path from every other node in the network to the terminal node, which can be accomplished using algorithm 1.

Note that it is possible to use the same ideas developed in the previous section to track the best k paths from a start region to a terminal region. Given the optimal path $\pi^* = \{s = x_{-1}, x_0, \cdots, x_{N-1}, x_N = t\}$ connecting the start and end nodes s and t respectively, it is possible to compute the best alternative path from s to t. Note that nodes x_{-1} and x_N are infact "dummy nodes". To initialize the algorithm, insert a new node x'_N into the state space with $c(x'_N, x_N) = \infty$.

Definition 3 *Let P_x represent the neighborhood of node x. For any node $x_i, i \leq N-1$ along the optimal path π^*, define a new node x'_i such that $P_{x'_i} = P_{x_i} + \{x'_{i+1}\} - \{x_{i+1}\}$, and insert this node into the state space S. The cost of the transitions $c(x'_i, j) = c(x_i, j), for j \in P_{x_i} \cap P_{x'_i}$ and $c(x'_i, x'_{i+1}) = c(x_i, x_{i+1})$.*

The optimal cost $J(x'_i, x_N)$ from the newly inserted node x'_i to the terminal node x_N is given by

$$J(x'_i, x_N) = \min_{j \in P_{x'_i}} \{c(x'_i, j) + J(j, x_N)\}, \tag{2.15}$$

and the optimal path is simply the path that results in this minimum cost.

Proposition 4 *The optimal cost from node x'_i to node x_N is the best alternative path cost from node x_i to node $x_N, i \leq N-1$.*

Proof *The proof is by induction on i. Consider the case where $i = N-1$. The best alternative path cost from x_{N-1} to x_N is obtained by searching over all node $j \in P_{x_{N-1}} - \{x_N\}$ and minimizing the quantity $c(x_{N-1}, j) + J(j, x_N)$. However, since $P_{x'_{N-1}} = P_{x_{N-1}} - \{x_N\}$, the proposition holds for this case. Suppose the proposition is true for $i = k$, consider when $i = k-1$. The best alternative path cost from x_{k-1} to x_N must either pass through x_k or not pass through x_k. If $J_2(x_k, x_N)$ is the best alternative path from x_k to x_N, then the best alternative path cost from x_{k-1} to x_N is given by*

$$\min \left(\min_{j \in P_{x_{k-1}} - \{x_k\}} (c(x_{k-1}, j) + J(j, x_N)), c(x_{k-1}, x_k) + J_2(x_k, x_N) \right). \tag{2.16}$$

Now from the inductive hypothesis, $J_2(x_k, x_N) = J(x'_k, x_N)$, and $P_{x'_{k-1}} = P_{x_{k-1}} + \{x'_k\} - \{x_k\}$, so the induction is complete. As a result the proposition holds.

From Proposition 4, it is possible to compute the best alternative to the optimal path from a starting set of nodes to an ending set of nodes in the volume by choosing $i = -1$. Note that the best alternative to the optimal path is represented by the optimal path from the start node x_{-1} to a derivative of the terminal node x'_N. Now in order to compute the subsequent best alternative path it is necessary to repeat the process to find the best alternative path to the optimal path between x_{-1} and x'_N. By iteratively repeating this process, it is possible to compute the best k paths connecting start and terminal nodes x_{-1} and x_N, for any arbitrary k. As illustrated in [20], it is possible to further optimize this algorithm so that it requires less space. This algorithm is presented below.

Algorithm 2 *Define $\bar{x}_h$ to be the primed node x_h with no primes, $\hat{x}_{h+1}$ to be the node immediately subsequent to x_h along the path p, and $x_h^{(k)\prime}$ to be the node x_h with k primes. Determine the optimal path from every node in S to x_N, and let the optimal path from x_{-1} to x_N be p_1.*

Initialize $p = p_1$, $k = 1$ and add node x'_N to S

While an alternative to p exists and $k \leq K$

Set x_i = the first node before x_N along p

For every $x_j \in \{x_i, \cdots, x_{-1}^{(k-1)\prime}\}$

add node x'_j to S

update $P_{\bar{x}_j} = P_{\bar{x}_j} - \{\hat{x}_{j+1}\} + \{\hat{x}'_{j+1}\}$

set $J(x'_j, x_N) = \min_{n \in P_{\bar{x}_j}} \{J(n, x_N) + c(\bar{x}_j, n)\}$

end

set p = the optimal path from $x_{-1}^{(k)\prime}$ to x_N; $k = k + 1$

end

2.4 Surface Generation

Once the fibers have been reconstructed using the dynamic programming algorithm outlined before, they are embedded in a surface for visualization. For axonal fibers in the brain, a triangulated cortical surface is generated with an isosurface generation algorithm that uses tetrahedral decomposition.

In order to generate a triangulated surface, MR data is first segmented into five volumes using the Bayesian segmentation algorithm outlined in [23] and [24]. The five

volumes are meant to represent CSF, CSF/Gray matter (partial volume), Gray matter, Gray/White matter (partial volume), and White matter. Using the local parametric values from the Gray/White matter partial volume compartment in the segmentation, the cortical surface is generated using the isosurface algorithm described in [21], [22], [23]. Fig. 2.5 illustrates regions of the cortical surface generated using this technique.

(a) (b)

Figure 2.5: Isosurfaces generated using tetrahedral decomposition algorithm. (a) An illustration of the cortical surface. (b) An illustration of the prefrontal gyrus extracted from the surface.

Chapter 3

Validation of Algorithm and Results

3.1 Phantom Data Sets

In order to ensure that the algorithm performs accurately phantom images and diffusion tensor data are used to test the validity of the algorithm. The results of tracing a path from a starting point to an end point with various 2 dimensionsal and 3 dimensionsal phantom data are presented. By examining these results, it can be show that the generated paths are in fact the minimum energy paths connecting the start and end points.

For this purpose three categories of phantom data sets were generated. Each voxel has an ellipsoid associated with it. As previously defined the energy associated with moving from one voxel to an adjacent voxel as being the inverse of the distance between the center of the ellipsoid and the surface of the ellipsoid in the direction of the neighboring voxel. For the first category of phantom data sets, all voxels in the image were assigned ellipsoids that differed only in their size and were identical with respect to their directionality and anisotropy. Hence the energy associated with moving to an adjacent voxel from a voxel with a large ellipsoid is much lower than moving to the corresponding adjacent voxel from a voxel with a small ellipsoid. Hence paths generated using such data sets should move along regions in the image with large ellipsoids.

For the second category of data sets, each voxel in the image was assigned ellipsoids that differ only with respect to the direction of the major axis. All ellipsoids are identical in

shape and size, but are differently oriented in space depending of the position of the voxel associated with it. As a result if a path is traced between two voxels, the path should pass through regoins in the image whose ellipsoids are oriented towards the terminal voxel and should stay away from regions whose ellipsoids are oriented away from the terminal voxel.

In the third category of phantom data, the principal direction and the volume of the ellipsoids are held constant, while the anisotropy of the ellipsoids is varied. The purpose of this phantom data set is to simulate real data. In an actual diffusion tensor MRI of the human brain, it is believed that regions of high anisotropy in the image correspond to nerve fibers in the brain. It is know that an ellipsoid with anisotropy in a given direction corresponds to a low energy associated with moving in that direction. In addition, as the energy is additive, paths that minimize this energy should move towards regions with high anisotropy values in the direction of the terminal point.

3.1.1 Eigenvalue Variation

This section presents the results of tracing minimum energy paths on 2D and 3D phantom data sets (Fig. 3.1) in which all voxels possess ellipsoids whose direction and anisotropy are identical, but whose size varies. We already know that the energy corresponding to moving from a voxel, in a particular direction depends upon the ellipsoid associated with that voxel. In particular, this energy is inversely proportional to the distance between the center of the ellipsoid and the surface of the ellipsoid in the given direction. Hence, all voxels in the image are assigned ellipsoids that vary only by some constant scale factor, minimum energy paths should tend to pass through regions with large ellipsoids. This is because larger ellipsoids correspond to lower costs as the distance between the ellipsoid center and surface in a given direction is greater than for a smaller, yet otherwise identical ellipsoid.

3.1.2 Eigenvector Variation

Another factor which affects the costs of paths in particular direction is the orientation of the ellipsoids associated with each voxel. This section presents paths generated from synthetic diffusion tensor data in which all voxels have ellipsoids that are oriented differently. Apart from the orientation, all ellipsoids are identical in size and anisotropy. As a result paths passing through the voxels will have an affinity towards the direction associated with the highest eigenvalue. So to test the algorithm, set the direction associated with the highest

eigenvalue of most of the voxels to be perpendicular to the direction between start and end points. Also there are a small set of voxels whose directions of the largest eigenvalue are not perpendicular to the direction between start and end points. In addition, the ellipsoids are ensured to be highly anisotropic, so that paths passing through the first set of voxels described above have high costs. Thus, it should be expected to see paths that try to minimize the passage through these voxels. Fig. 3.2 illustrates the result of the algorithm through 2D and 3D phantom data sets.

3.1.3 Anisotropy Variation

The degree of anisotropy of the diffusion tensor ellipsoids also have an effect on the cost function. In diffusion tensor images of the brain and heart, it is thought that directions of higher anisotropy reflect fiber direction [26], [32]. In this phantom data set, the anisotropy of the ellipsoids are varied while the eigenvectors remain fixed. If the directions associated with the largest eigenvalue are oriented towards the end point, paths generated should tend to pass through the regions of higher anisotropy. 2D and 3D data sets, along with paths are shown in Fig. 3.3.

3.2 Results

3.2.1 Anisotropy Index

Once the validity of the algorithm was ascertained, fibers were tracked using human brain and heart diffusion tensor data. A single diffusion tensor MR data set consisting of an MR image of a human brain and a 3×3 tensor value for each voxel in the image was analyzed and various paths were tracked. Once the eigenvalues and eigenvectors were calculated for this data set, a cylindrical anisotropy index [27] was calculated for each voxel, defined as

$$A_{cyl} = \frac{\lambda_1 - (\lambda_2 + \lambda_3)/2}{\lambda_1 + \lambda_2 + \lambda_1} \tag{3.1}$$

There is significant evidence to suggest that this anisotropy index reflects the degree of fiber density and myelination of neuronal projections [26]. Hence reconstructed pathways should pass through regions associated with high anisotropy index. Fig. 3.4 shows this anisotropy map, highlighting the major regoins in which fibers were tracked.

3.2.2 Cortical Neuronal projections

In the human brain the corpus callosum is a thick band of fibers known as the commisural fibers, located between the cerebral hemispheres [3], [4]. This structure is the primary connection between the left and right hemispheres of the brain, and as a result any path traced from one hemisphere to another should traverse along the corpus callosum. We traced paths through the body of the corpus callosum with starting and ending points in each hemisphere. The result of one particular tracking experiment is shown in Fig. 3.5 and as expected, the paths connecting regions in different hemispheres passed through the corpus callosum [30].

In addition to the corpus callosum, another area of interest are fibers passing through the internal capsule. The internal capsule is the major structure carrying ascending and descending projection fibers to and from the cerebral cortex [4], [28], [29]. We attempted to track fibers from the Ventral Posterolateral Nucleus (VPL) of the Thalamus, to various regions in the Somatosensory Cortex. It is known that fibers of the sensory pathways that transmit sensory information to the somatosensory cortex, pass through the posterior limb of the internal capsule [4]. The paths produced by the dynamic programming algorithm (Fig. 3.6) are consistent with this anatomy.

A third set of neuronal projection that were reconstruct, are the geniculo-calcarine visual pathways that connect the lateral geniculate nucleus with the visual cortex, near the calcarine sulcus. These fibers are responsible for relaying visual information from the thalymus to the visual cortex. Consistent with known anatomy the fibers generated were tracked in a posterior direction from the LGN and ran parallel to the occipital horns of the lateral ventricle [4]. One such fiber can be seen in Fig. 3.7.

The best K fibers linking regions in the brain were also computed using algorithm 2 and compared to similar fibers generated using principal eigenvalue thresholding. The fibers tracked and compared were the posterior and anterior thalamic radiations, passing horizontally through the internal capsule. The anterior thalamic radiations are thought to connect the frontal lobe of the brain with the medial and anterior thalamic nuclei, and are known to pass through the anterior limb of the internal capsule [5]. The posterior thalamic radiations connect the posterior and occipital regions of the brain with the caudal portions of the thalamus. Included in this bundle is the optic radiation which travels from the LGN to the calcarine cortex [5]. The results of tracking the anterior thalamic radiations using

both principal eigenvalue thresholding and dynamic programming are shown in Fig. 3.8, and those for the posterior thalamic radiations are illustrated in Fig. 3.9. The paths created with principal eigenvalue thresholding were based on techniques described in [27]. The paths generated by each algorithm is generally consistent with known anatomy, though there are some distinct differences between the two sets of paths. The best K paths generated through the dynamic programming algorithm linking two regions are more closely bundled than the paths generated with principal eigenvalue thresholding, indicating that the optimal paths are bundled together and then branch to reach the terminating node. The fiber paths become less bundled as the value of K is increased. For this experiment a value of $K = 2000$ was used, and the fibers produced were more bundled than those produced from the principal eigenvalue thresholding, which number between 200 and 450. Paths generated using principal eigenvalue thresholding are computed by bidirectionally tracking the principal eigenvector of the diffusion tensor matrix, terminating when the anisotropy falls below a certain threshold. This threshold is usually still in the white matter range, and as a result it becomes difficult to track paths near gray matter regions. In the case of the dynamic programming algorithm, the starting and ending regions are specified as constraints for the paths and thus tracking of paths in regions of low anisotropy is feasable.

3.2.3 Myocardial Fibers

Diffusion tensor MRI data of the heart was also obtained, and myocardial fibers were reconstructed using the dynamic programming method. It is thought that the walls of the ventricles are composed of a continuum of fibers that sweep towards the apex of the heart at the epicardial surface. The fibers also gradually undergo a 180^o change in orientation while passing from the epicardium to the endocardium. Hence the epicardium fibers are parallel but opposite in direction to the endocardium fibers, while fibers in the midwall lie perpendicular to these. The anatomic structure of the myocardial fibers is described in detail in [33], [32], and [7]. Shown in Fig. 3.10 is the anisotropy map for the heart data set. The epicardial and endocardial walls of both the right and left ventricles exhibit a higher anisotropy index than the midwall, indicating higher fiber density in these regions. This is in agreement with [33]. As a result of the geometry of the myocardial fibers, any paths tracked from the epicardium of the heard towards the endocardium would be expected to stay in the horizontal or image plane. The result of tracking such fiber paths

on the free wall of the left ventricle is shown in Fig. 3.10. As expected, the paths of the deviate very little from the image plane.

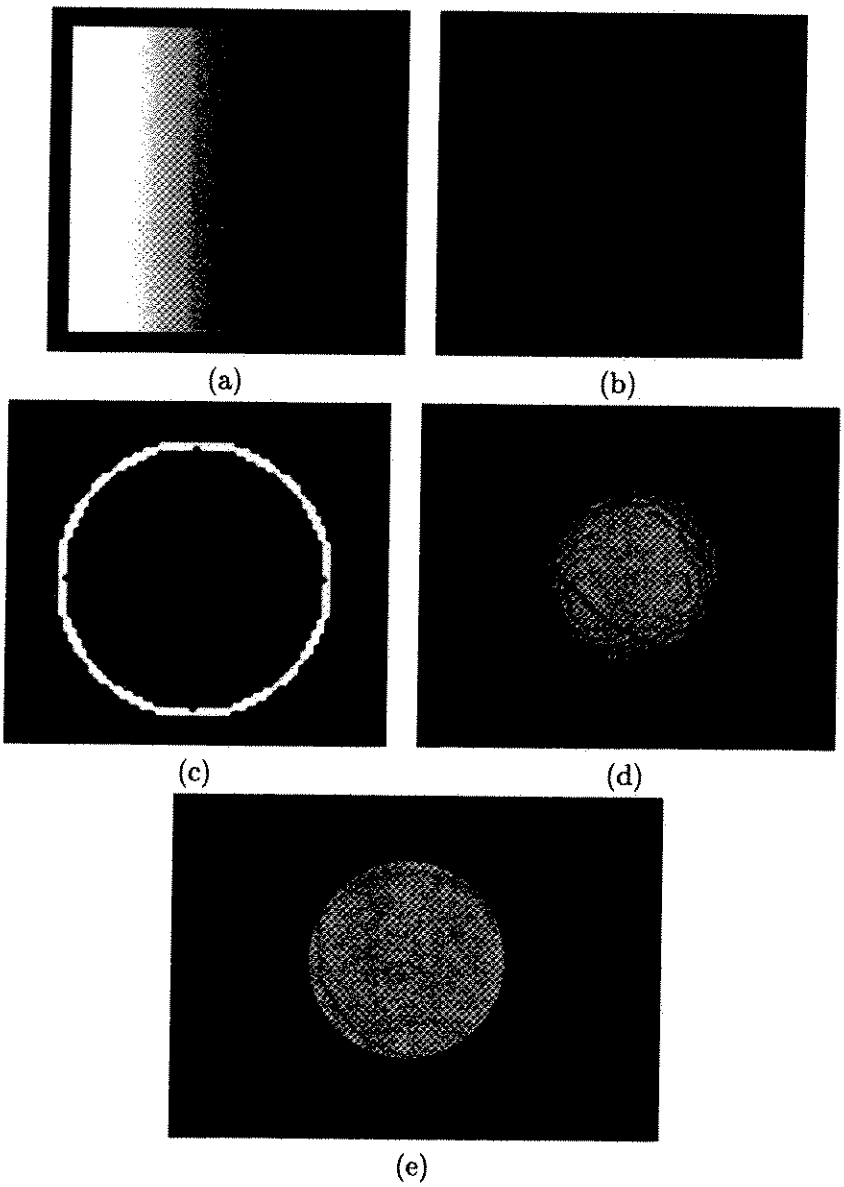

Figure 3.1: 2D and 3D phabtom data sets in which all ellipsoids are sphereical, with varying radii. (a) Illustration of the radii of each voxel of the 2D phantom, with white corresponding to a radius of 256 and black corresponding to a radius of 1. (b) Three paths of minimum energy through this phantom space. (c) Slice through a spherical shell 3D phantom. White represents spheres each with raduis 10 and black represents spheres with radius 1. (d)Three paths of minimum energy are depicted relative to the inner surface of the spherical shell. Note that these paths pass along this surface. (e)The same thre minimum energy paths shown embedded in the outer surface of the spherical shell. This view clearly shows that the paths pass through the regions of the image with large spheres associated with the voxels.

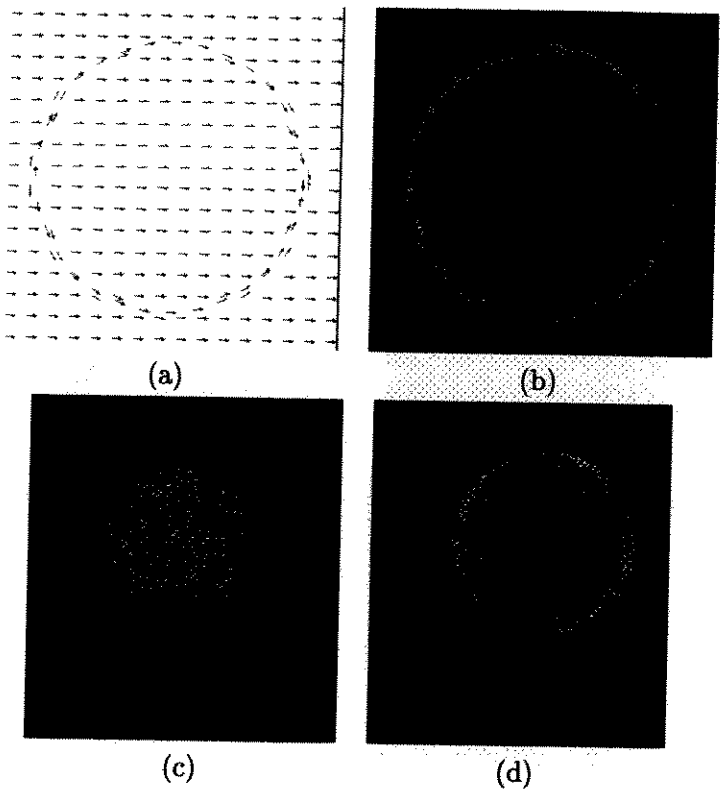

Figure 3.2: 2D and 3D phantom data sets in which ellipsoids are identical in shape but vary in orientation. (a)The vector field illustrating the direction corresponding to the largest eigenvalue of a sample of voxels in a 2D phantom. (b) Three paths of minimum energy. Paths passing through voxels not lying on the circle have higher energies associated with them. Note that all paths shown here minimize passage through voxels not on the circle. (c) Illustration of a minimum energy path of the 3D phantom data with elliposoids on the shpere oriented such that their principal axes are tangential to the sphere. The paths are shown on the inner surface of the spherical region. (d) Illustration of the same minimum energy path shown embedded in the outer surface of the spherical region. Note that the path minimizes the passage through voxels not on the sphere.

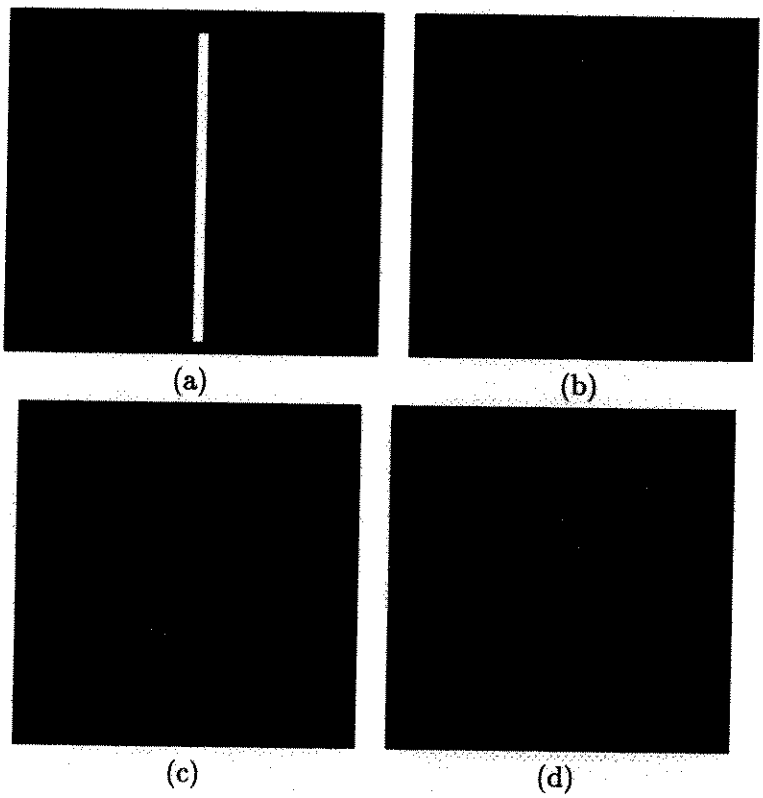

Figure 3.3: (a) Anisotropy map showing regions of high anisotropy. For each voxel, the direction of highest anisotropy is vertical and the white regions have a high anisotropy value, while dark regions have a significantly lower anisotropy value. (b) Three minimum energy paths. Note that the path tends to move along the region of high anisotropy. (c) 3D anisotropy map showing regions of high anisotropy. The direction of highest anisotropy is the same for all voxels in the image. (d) Paths of minimum energy tend to move along the region of high anisotropy.

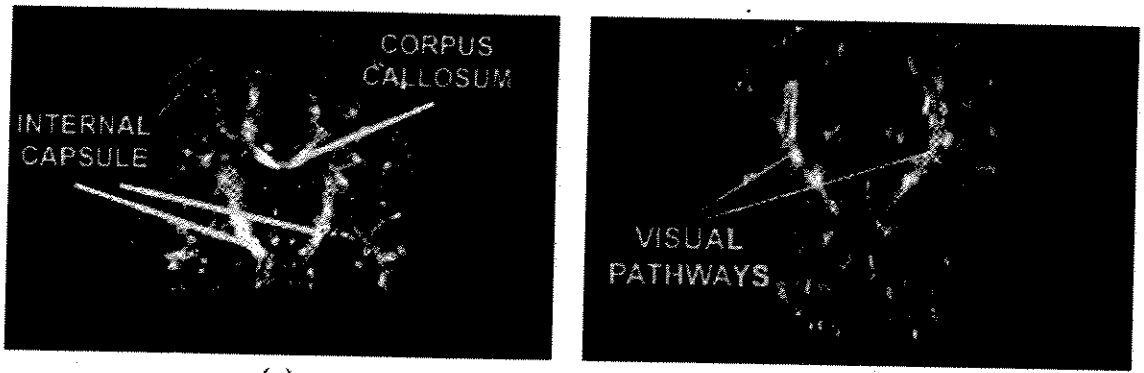

(a) (b)

Figure 3.4: Anisotropy map of the brain showing regions of high anisotropy. (a) Axial view. (b) Coronal view

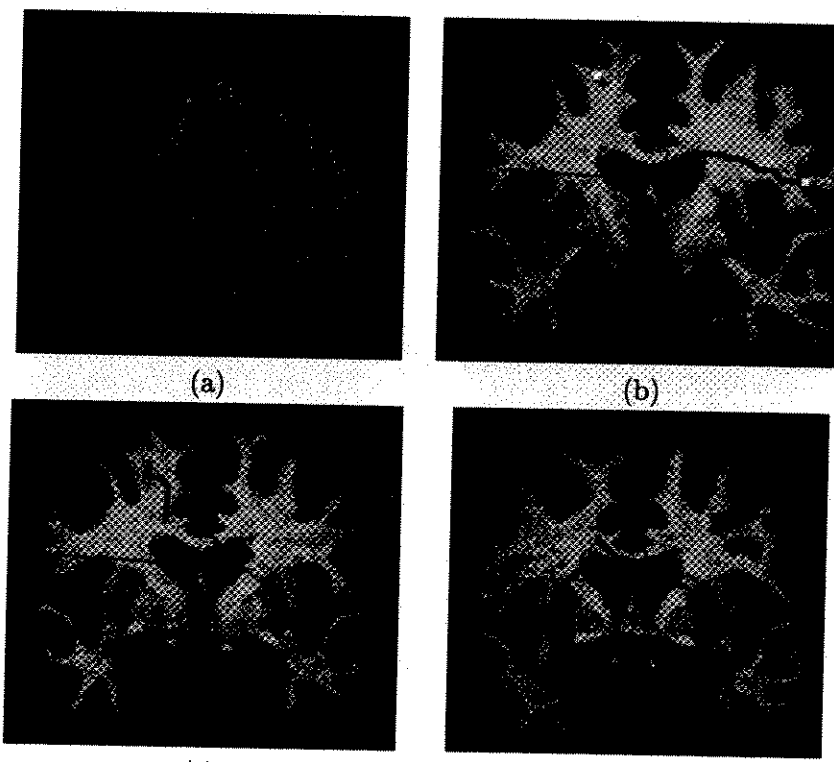

(a) (b)

(c) (d)

Figure 3.5: A path through the body of the corpus callosum. (a) The fiber is embedded in a surface reconstruction of the cortex. (b)-(d) The fiber and cortical surface are embedded in the MR volume.

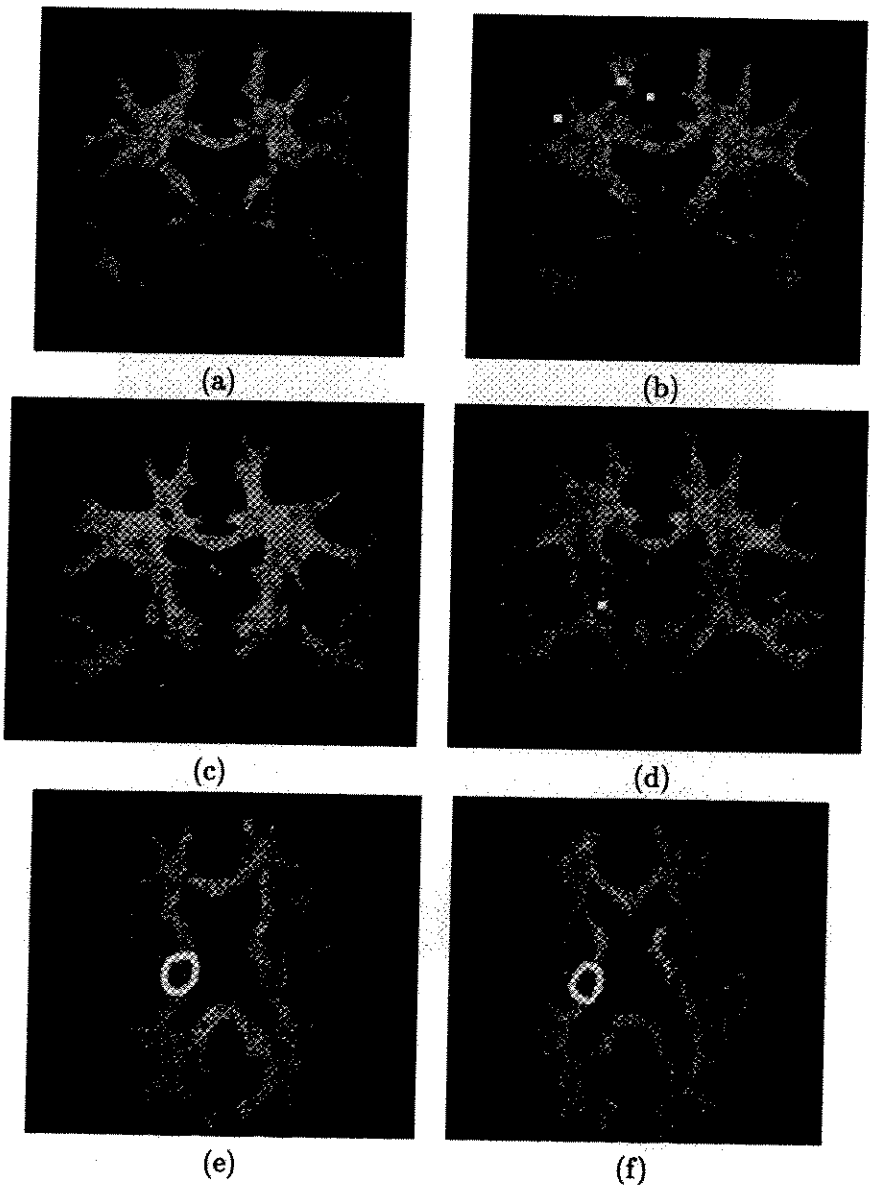

Figure 3.6: Slices depicting paths ascending through the posterior limb of the internal capsule. (a)-(d) depict the paths as seen in the axial view, ascending from the Ventral Posterolateral Nucleus (VPL) of the Thalamus, to the Somatosensory cortex through the internalcapsule. (e)-(f) illustrate the paths as seen in the coronal view, clearly passing through the posterior limb of the internal capsule.

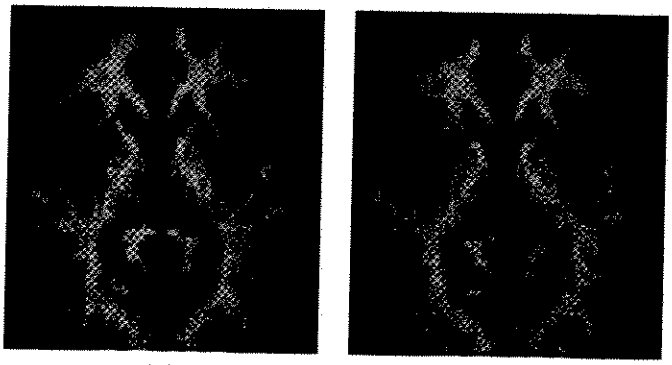

(a) (b)

Figure 3.7: A reconstruction of the geniculo-calcarine pathways linking the lateral geniculate nucleus with the visual cortex close to the calcarine sulcus.

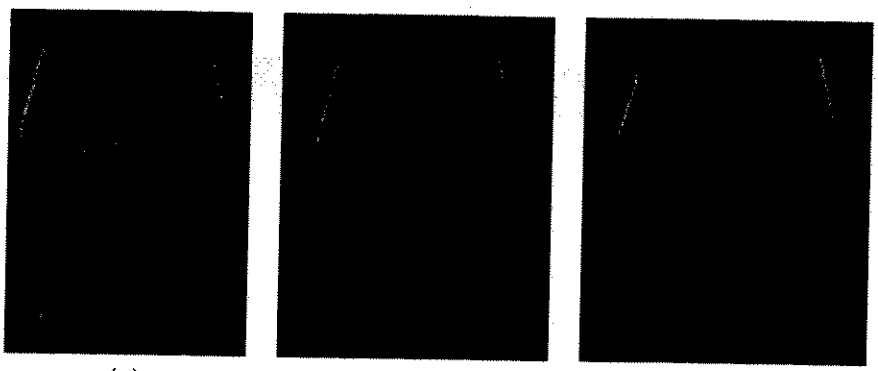

(a) (b) (c)

Figure 3.8: Anterior thalamic radiations. (a)-(b) Slices showing the paths generated using dynamic programming (c) A slice showing paths generated using principal eigenvalue thresholding.

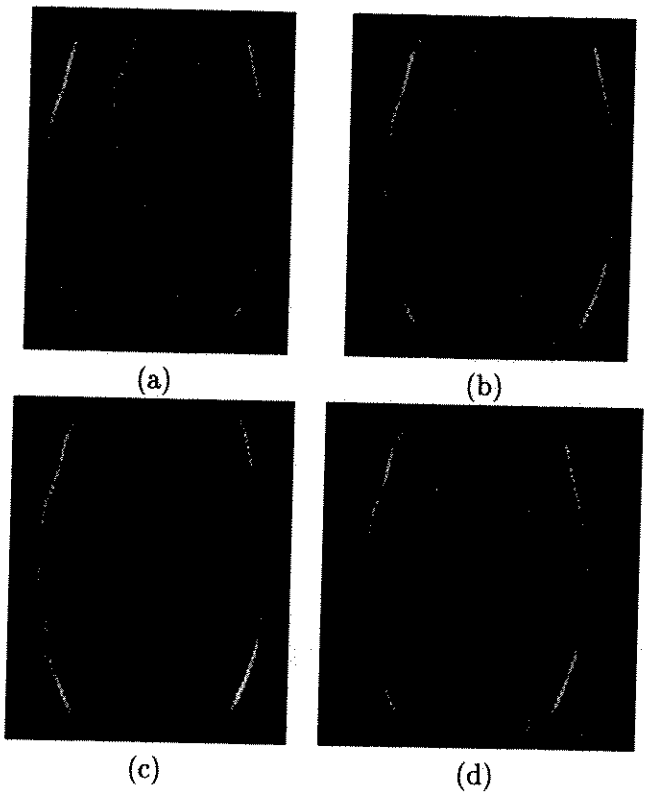

Figure 3.9: Posterior thalamic radiations. (a)-(c) Slices showing the paths generated using dynamic programming (d) A slice showing paths generated using principal eigenvalue thresholding.

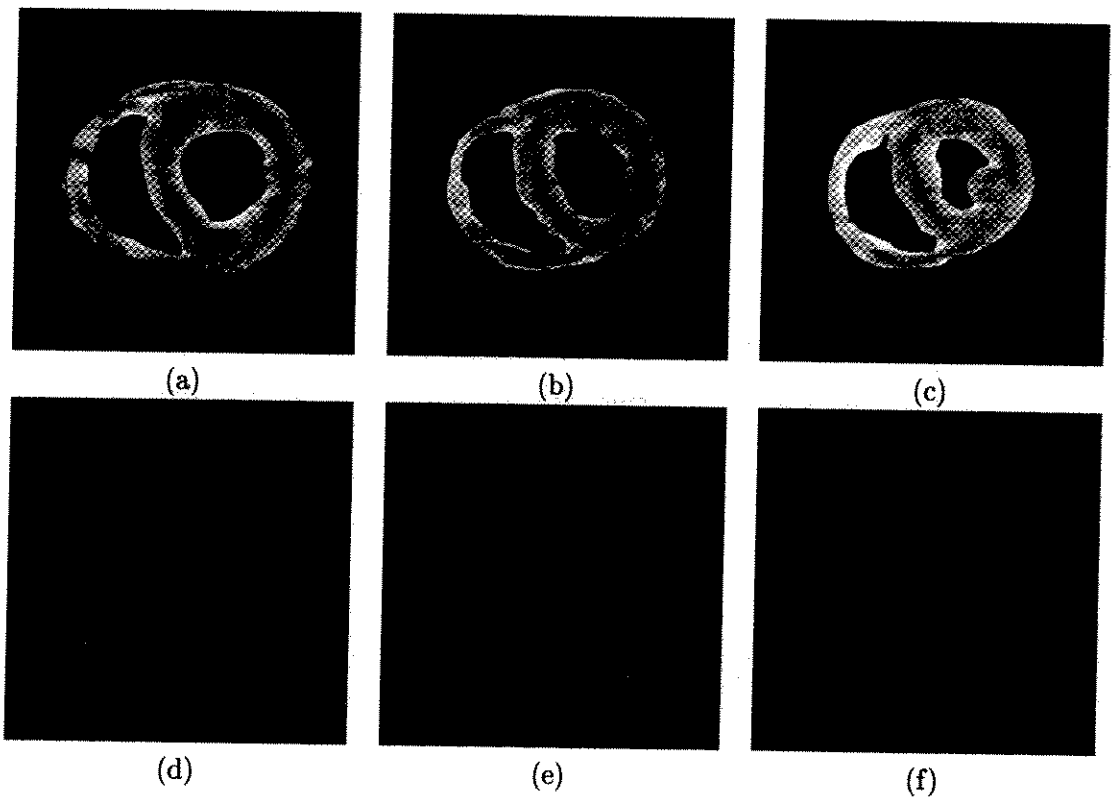

Figure 3.10: Heart data set. (a)-(c) Anisotropy map of the heart diffusion tensor data. (d)-(f) Myocardial reconstructions of the free wall of the left ventricle. Fibers were tracked from the epicardium to the endocardium.

Chapter 4

Frenet Curve Representation

4.1 Curvature and Torsion

The curves generated by the dynamic programming algorihtm simply minimize an energy function derived from the diffusion tensor associated with each voxel in the image. These curves do not utilize any prior knowledge of the geometry of the fibres in the brain. Knowledge of Frenet characteristics such as average curvature and average torsion of fibers can be incorporated into the cost function of the dynamic programming algorithm [13] to produce a more realistic representation of the fibers.

The *curvature* of a unit speed curve $\alpha(s)$ parametrized by arc length can be described as a measure of the rate of change of the tangent vector at s. The second derivative of the curve can be written as, $\alpha''(s) = \kappa(s)n(s)$, where $n(s)$ is a unit vector and is called the *normal vector*. The unit vectors $\alpha'(s)$ and $n(s)$ define what is called the *osculating plane*. The unit normal to this plane $b(s)$ is called the *binormal vector* at s.

Definition 4 *Let $\alpha : I \to R^3$ be a curve parametrized by arc length $s \in I$. If the second derivative is written as $\alpha''(s) = \kappa(s)n(s)$, the magnitude $\kappa(s)$ is called the curvature of α at s.*

Proposition 5 *The tangent vector $t(s) = \alpha'(s)$ is perpendicular to the normal vector $n(s)$.*

Proof By differentiating the equation $\alpha'(s) \cdot \alpha'(s) = 1$, we get

$$\begin{aligned} & \alpha'(s) \cdot \alpha''(s) + \alpha''(s) \cdot \alpha'(s) = 0 \\ \Rightarrow \quad & \alpha''(s) \cdot \alpha'(s) = 0 \\ \Rightarrow \quad & \kappa(s) n(s) \cdot t(s) = 0. \end{aligned}$$

Hence $t(s) \perp n(s)$. □

Proposition 6 *The derivative of the binormal vector $b'(s)$ is parallel to the normal vector $n(s)$.*

Proof Recall that $b(s) \perp b'(s)$ and that $t(s)$, $n(s)$, and $b(s)$ are mutually orthonormal. Now, $b'(s) \perp t(s)$ since,

$$\begin{aligned} b'(s) &= \frac{d}{ds}[t(s) \times n(s)] \\ &= t'(s) \times n(s) + t(s) \times n'(s) \\ &= t(s) \times n'(s) \end{aligned}$$

Hence $b'(s) \parallel n(s)$ and $b'(s) = \tau(s) n(s)$. □

Definition 5 *Let $\alpha : I \to R^3$ be a curve parametrized by arc length $s \in I$. If the derivative of the binormal vector is written as $b'(s) = \tau(s) n(s)$, the magnitude $\tau(s)$ is called the torsion of α at s.*

To implement an algorithm that computes the local curvature and torsion of curves in R^3 efficiently, a more mathematically explicit formulation of these parameters is required. To achieve this, consider the Frenet representation of these curves [13], [14], [15] which gives rise to what is known as the Frenet formulas.

Proposition 7 *The Frenet formulas are defined as*

$$t'(s) = \kappa(s) n(s) \tag{4.1}$$

$$n'(s) = -\kappa(s) t(s) - \tau(s) b(s) \tag{4.2}$$

$$b'(s) = \tau(s) n(s) \tag{4.3}$$

Proof From Definition 1, $\alpha''(s) = \kappa(s)n(s) = t'(s)$. Hence Equation 4.1 holds.
From Definition 2, $b'(s) = \tau(s)n(s)$. Hence Equation 4.3 holds.
Since $n(s) = b(s) \times t(s)$,

$$\begin{aligned} n'(s) &= b'(s) \times t(s) + b(s) \times t'(s) \\ &= -\tau(s)b(s) - \kappa(s)t(s) \end{aligned}$$

Hence Equation 4.2 holds. □

Proposition 8 *As per the Frenet representation, if $x(\cdot)$ is a unit speed curve parametrized by arc length, then the curvature field, κ, is given by*

$$\kappa(s) = \sqrt{\left[\frac{d^2x_1(s)}{ds^2}\right]^2 + \left[\frac{d^2x_2(s)}{ds^2}\right]^2 + \left[\frac{d^2x_3(s)}{ds^2}\right]^2} \tag{4.4}$$

Proof From Definition 1, $\kappa(s) = \|\alpha''(s)\|$. Hence Equation 4.4 holds. □

Proposition 9 *As per the Frenet representation, if $x(\cdot)$ is a unit speed curve parametrized by arc length, then the torsion field, τ, is given by*

$$\tau(s) = \frac{1}{\kappa^2(s)} \begin{vmatrix} \frac{dx_1(s)}{ds} & \frac{dx_2(s)}{ds} & \frac{dx_3(s)}{ds} \\ \frac{d^2x_1(s)}{ds^2} & \frac{d^2x_2(s)}{ds^2} & \frac{d^2x_3(s)}{ds^2} \\ \frac{d^3x_1(s)}{ds^3} & \frac{d^3x_2(s)}{ds^3} & \frac{d^3x_3(s)}{ds^3} \end{vmatrix} \tag{4.5}$$

Proof It can easily be seen that the right hand side of Equation 4.5 reduces to $t(s) \cdot (n(s) \times n'(s))$. From Equation 4.2 we get that

$$\begin{aligned} t(s) \cdot (n(s) \times n'(s)) &= t(s) \cdot (n(s) \times (-\tau(s)b(s) - \kappa(s)t(s))) \\ &= t(s) \cdot (\tau(s)t(s) - \kappa(s)b(s)) \\ &= \tau(s) \end{aligned}$$

□

Equations 4.4 and 4.5 now allow for the efficient computation of local curvature and torsion of curves in R^3, as long as the curve is smooth and differentiable. In the case of fiber projections, the tracking algorithm outlined in Chapter 2 generates a fiber that is a collection of discrete points in R^3, corresponding to voxels through which the fiber passes. The computation of curvature and torsion directly depends on the derivatives of the curve. Thus, in order for the derivatives to be valid it is necessary to fit the set of points defining the fiber with a smooth and continuous spline curve. The next section details the choice of the spline fit and its implementation.

4.2 Theory of Splines

4.2.1 Natural Cubic Splines

Cubic splines are obtained by fitting a given set of control points with a piecewise cubic polynomial curve that passes through each point. One class of cubic spline interpolation curves is the natural cubic spline. Given a set of $n+1$ control points, it is possible to describe a parametric cubic polynomial that is fitted between each pair of control poits.

$$x(u) = a_x u^3 + b_x u^2 + c_x u + d_x \tag{4.6}$$

$$y(u) = a_y u^3 + b_y u^2 + c_y u + d_y \tag{4.7}$$

$$z(u) = a_z u^3 + b_z u^2 + c_z u + d_z \tag{4.8}$$

where $0 \leqslant u \leqslant 1$.

This set of equations yields $4n$ polynomial coefficients that need to be determined. At each of the $n-1$ internal points, there are four boundary conditions. The two curve sections on either side of the point must have the same first and second derivative, and both curve sections must pass through the point. Two more conditions that must be satisfied are that the curve must pass through the start and end points also. This gives $4n-2$ conditions that must be satisfied. One method of obtaining two more constraints so as to be able to compute values for all coefficients is to set the derivatives of the curve at the start and end points to zero. Solving these equations for the polynomial coefficients completely defines the natural spline curve.

One major disadvantage of using natural spline curves is that all control points are needed to compute the spline fit, and as a result it is not possible to compute local fits without knowledge of all the control points. If spline curves are to be used to compute the local curvature and torsion values of fibres and incorporated into the dynamic programming tracking algorithm, then the ability to compute local curvature and torsion without knowledge of the entire path is imperative. Hence natural spline curves cannot be used in this case, but they provide a basis upon which other spline interpolation techniques are built.

4.2.2 Cardinal Splines

Cardinal splines are also piecewise cubic polynomials used to fit a set of control points, but each polynomial can be completely specified from only four consecutive control points and

does not depend on the entire set of control points. This allows for greater flexibility in terms of the computation of local curvature and torsion as these can be computed without the entire set of control points. Each polynomial (Equations 4.6, 4.6, and 4.6) consists of four unknowns, and the conditions that these polynomials satisfy are given by

$$\begin{aligned} P(0) &= p_k \\ P(1) &= p_{k+1} \\ P'(0) &= \frac{1}{2}(1-t)(p_{k+1} - p_{k-1}) \\ P'(1) &= \frac{1}{2}(1-t)(p_{k+2} - p_k) \end{aligned}$$

Hence the slopes atcontrol points p_k and p_{k+1} are assumed to be proportional to the chords $\overline{p_{k-1}p_{k+1}}$ and $\overline{p_k p_{k+2}}$ respectively (Fig. 4.1). The parameter t is called *tension*. See Fig. 4.2 for an illustration of the effect of this parameter. In fitting the fiber tracking data, a value of $t = 0$ was used.

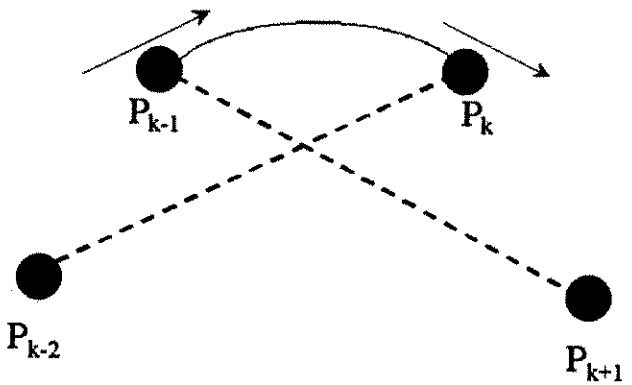

Figure 4.1: Boundary conditions in a cardinal spline curve fit. Tangent vectors at end points are proportional to the chords formed by neighboring control points.

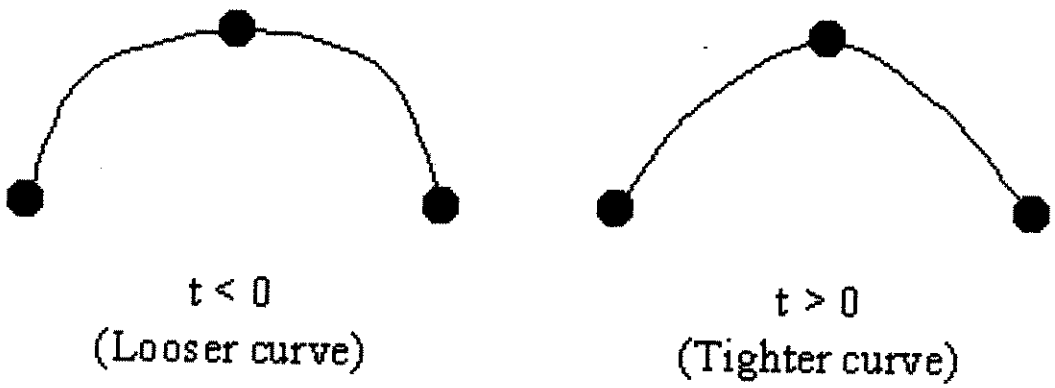

Figure 4.2: Illustration of the tension parameter in a cardinal spline curve fit.

4.3 Application to Dynamic Programming

4.3.1 Frenet Analysis of Fibers

Apart from the possibility of containing noise, resolution of diffusion tensor data is not high enough to isolate individual fibers. Actually, there may be many fibers running through a given voxel, and the eignevectors of the diffusion tensor matrix can only measure the average effect of all fibers. As described in earlier sections, incorporation of prior information about the characteristics of neuronal fibers into the tracking algorithm is desirable as it reduces the dependence of the algorithm on the diffusion tensor data. Understanding the Frenet properties of curvature and torsion of fiber curves also serves as a useful tool to compare fiber paths obtained through computation and through other invasive techniques.

Fig. 4.3 depicts a fiber curve generated through the use of the dynamic programming algorithm. This curve consisted of a set of discrete lattice points, and in order to compute curvature and torsion, it was necessary to fit the data using cardinal spline interpolation. Once this was done, the curvature and torsion at each discrete lattice point on the fiber was calculated according to Equations 4.4, and 4.5.This analysis is presented in Fig. 4.3. Using these curvature and torsion plots it is possible to define an L_1 norm that characterizes the distance between a curve, and some other template curve. This distance is given by

$$d_\kappa = \sqrt{\frac{\sum_{k=1}^{N} (\kappa_k - \bar{\kappa}_k)^2}{N}} \tag{4.9}$$

$$d_\tau = \sqrt{\frac{\sum_{k=1}^{N} (\tau_k - \bar{\tau}_k)^2}{N}} \tag{4.10}$$

Table 4.1 illustrates the curvature L_1 distance as well as the torsion L_1 distance between the fiber curve shown in Fig. 4.3 with a phantom template curve.

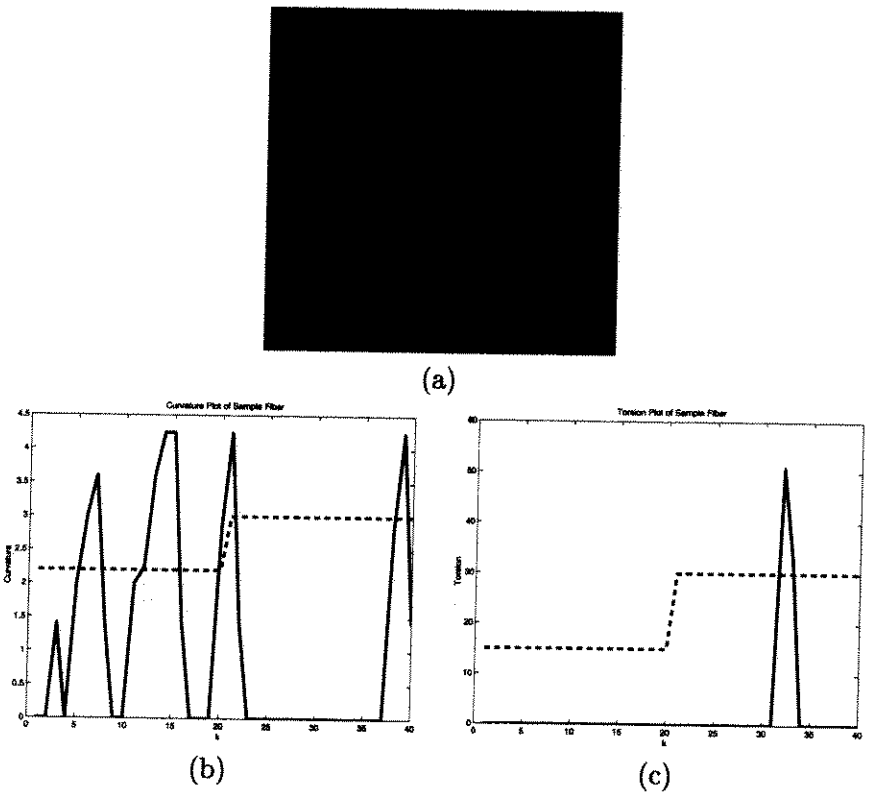

(a) (b) (c)

Figure 4.3: (a) Illustration of a sample fiber path, running through the corpus splenium. (b) A plot depicting the curvature at each point along the fiber (solid), along with curvature values for a phantom template (dash). (c) A plot depicting the torsion at each point along the fiber (solid), along with torsion values for a phantom template (dash).

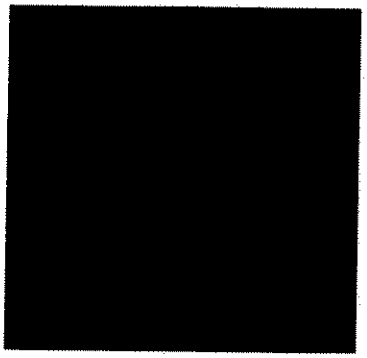

(a)

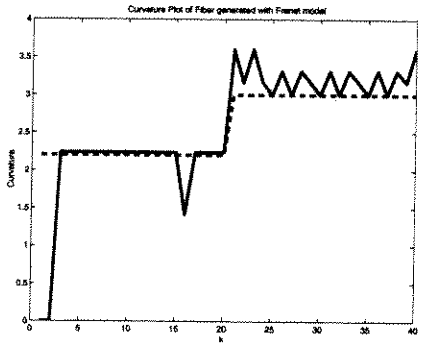

(b)

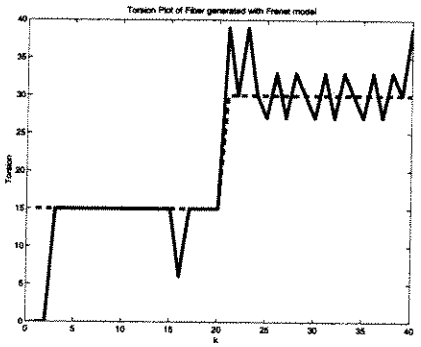

(c)

Figure 4.4: (a) Illustration of a fiber path with the same start and end points as in Fig. 4.3, but generated using the Frenet model for fibers. (b) A plot depicting the curvature at each point along the fiber (solid) in (a), along with curvature values for a phantom template fiber (dash). (c) A plot depicting the torsion at each point along the fiber (solid) in (a), along with torsion values for a phantom template fiber (dash).

4.3.2 Modification of Cost Function

With the curvature and torsion of a curve given by Equations 4.4, and 4.5 it is possible to associate an additional energy function with differences in curvature and torsion between a generated fiber and a template fiber. For the prior distribution, define the potential energy associated with the mean curvature and torsion $\bar{\kappa}, \bar{\tau}$ with the N-length paths of the template fiber, assuming constant inverse variabilities α, β as

$$\mathcal{U}(\kappa, \tau) = \alpha \sum_{k=1}^{N} (\kappa_k - \bar{\kappa}_k)^2 + \beta \sum_{k=1}^{N} (\tau_k - \bar{\tau}_k)^2 \tag{4.11}$$

In the current implementation of the algorithm, the mean curvature and torsion along with

their variabilities are left as parameters that the user can set, since accurate template fibers were not available. However, analysis in which phantom values are assigned as template curvature and torsion is presented so as to provide a framework to understand how estimated mean curvature and torsion values would be used in conjunction with the dynamic programming algorithm in the event that accurate template data from other (perhaps invasive) imaging sources becomes available.

The empirical estimates of the mean curvature and torsion and their variabilities would be defined for similarly shaped fibers, according to the formulas

$$\hat{\bar{\kappa}}_k = \frac{1}{M}\sum_{m=1}^{M}\kappa_k^{(m)}, \hat{\bar{\tau}}_k = \frac{1}{M}\sum_{m=1}^{M}\tau_k^{(m)} \tag{4.12}$$

$$\hat{\alpha}^{-1} = \frac{1}{MN}\sum_{m=1}^{M}\sum_{k=1}^{N}(\kappa_k^{(m)} - \hat{\bar{\kappa}}_k)^2, \hat{\beta}^{-1} = \frac{1}{MN}\sum_{m=1}^{M}\sum_{k=1}^{N}(\tau_k^{(m)} - \hat{\bar{\tau}}_k)^2 \tag{4.13}$$

where N is the length of the template fibers, and M is the number of fibers used in the estimate. In this experiment, the mean curvature and torsion at each point on the fiber is given by Fig. 4.3, and their variabilities were assigned values of 1.

The potential energy defined in Equation 4.11 was then incorporated into the cost function of the dynamic programming algorithm in order to accomodate prior information of the geometric properties of the fibers. The curvatures and torsions of the paths were calculated by first fitting cardinal splines [6] to the nodes of the fiber paths. The new cost function $E^k(x,y)$ between two points $x \in S_k$ and $y \in S_{k+1}$ is given by

$$E^k(x,y) = c^k(x,y) + \alpha\left(\kappa_k - \bar{\kappa}_k\right)^2 + \beta\left(\tau_k - \bar{\tau}_k\right)^2 \tag{4.14}$$

It should be noted however, that curvature and torsion estimates of an arc connecting two points on the path depend on other points comprising the path. In this implementation in which cardinal splines are first fitted to the data to compute the curvature and torsion values, these values depend on the two previous nodes along the path. Hence the cost defined in Eq. 4.14 also implicitly depends on these 4 points and for dynamic programming to generate the optimal solution, the state space of the algorithm has to be modified. In order for the cost function in Eq. 4.14 to depend only on nodes $x \in S_k$ and $y \in S_{k+1}$, the definition of a node has to be modified.

Definition 6 *Denote the center of any voxel in the volume to be a point. Define a node x to be a set of 3 points that correspond to 3 adjacent voxels in the volume, $x = \{p, q, r | q \in N_p, r \in N_q\}$, where N_v is the neighborhood of point v. A transition exists between nodes $x_i = \{p, q, r\}$ and node $x_{i+1} = \{q, r, s\}$ if $s \in N_r$. The cost of this transition is given by*

$$E^k(x_i, x_{i+1}) = c^k(r, s) + \alpha\left(\kappa_k(q, r, s, t) - \bar{\kappa}_k\right)^2 + \beta\left(\tau_k(q, r, s, t) - \bar{\tau}_k\right)^2. \tag{4.15}$$

With this changes to the state space, computing the optimal path between points s and t is now reduced to computing the optimal path between node $\mathbf{s} = \{s, s, s\}$ and $\mathbf{t} = \{t, t, t\}$.

Proposition 10 *For any node $x = \{p, q, r\} \in S_k$, denote P_x as the set of nodes $\{n = \{q, r, s\}\}$ such that $s \in N_r$. Define the cost $E^k(x_i, x_j)$ as in Eq. 4.15 for $x_j \in P_{x_i}$, and $E^k(x_i, x_j) = \infty$ for $x_j \notin P_{x_i}$. The optimal N-length cost $J_0(\boldsymbol{s})$ from $\boldsymbol{s}$ to $\boldsymbol{t}$ is given by the final step of the following algorithm evaluated at $i = \boldsymbol{s}$.*

Algorithm 3 *Initialize: $J_k(i) = \infty \quad i \neq \boldsymbol{t}$, $J_k(\boldsymbol{t}) = 0$ for all k; $S_N = \{\boldsymbol{t}\}$;*
For every $k = N - 1$ to 0,

$$S_k = \{i | i \in P_j, j \in S_{k+1}\}\text{; set } E^k(i, j),\ i \in S_k \text{ and } j \in S_{k+1}.$$

$$J_k(i) = \min_{j \in \{S_{k+1} \cap P_i\}} \{E^k(i, j) + J_{k+1}(j)\}, i \in S_k$$

end

Proof Proposition 2 holds since the cost function $E^k(i, j)$ is sequentially additive, and depends only on nodes $i \in S_k$ and $j \in S_{k+1}$.

Implementing the modified dynamic programming algorithm described in Algorithm 3 leads to a reduction in efficiency as the state space over which the search is performed is increased. Hence there is a trade off between *a priori* knowledge regarding mean curvature and mean torsion, and the optimality of the solution computed. To handle efficiency issues the current implementation does not use this increased state space algorithm and the optimal path search is carried out using the dynamic programming algorithm described in Algorithm 1. As a result the solution computed is an approximate.

Using this energy function which includes information about the prior knowledge of the Frenet properties of the fibers as the cost function, fiber curves were traced with the dynamic programming algorithm. Fig. 4.4 depicts the path, and its curvature and torsion plots along with the template curvature and torsion plots. Due to the quadratic

Fiber	Curvature L_1 Distance	Torsion L_1 Distance
Dynamic Programming	28.08	6.08
Frenet Model	2.08	1.61

Table 4.1: Curvature and Torsion L_1 distances between the fiber generated through the dynamic programming algorithm without prior Frenet information and template fiber, and between the fiber generated with the dynamic programming algorithm with prior Frenet information and the template fiber.

cost associated with inconsistencies in torsion, the newly generated curve has a high degree of torsion. Also, table 4.1 shows the curvature L_1 distance as well as the torsion L_1 distance between the fiber and the phantom template curve.

Chapter 5

Conclusion and Future Directions

The major contribution of this thesis was the extension of concepts based in the field of computational anatomy, particularly dynamic programming and the Frenet representation of curves, to solve the problem of tracking myocardial and cortical fibers using diffusion tensor imaging, as described in Chapter 2. The algorithm presented is based on dynamic programming, and similar to work done in curve extraction from brain surfaces [13], and boundary [10] and artery tracking [16], [17].

The primary advantage of this method over other current tracking techniques is that a globally optimal path linking two regions is obtained. Due to this fact the algorithm should be able to perform better than other thresholding algorithms in tracking paths through regions where the diffusion is relatively isotropic. The addition of Frenet properties to the algorithm also permits the reconstruction of more realistic fibers by accounting for prior knowledge of fiber characteristics of curvature and torsion.

To summarize, by using a dynamic programming algorithm and diffusion tensor imaging of human subjects, 3D representations of human cortical and myocardial neuronal projections were reconstructed. In addition to rigorously testing the algorithm on various phantom data sets, the commisural fibres through the corpus callosum, as well as fibers ascending through the internal capsule to regions in the somatosensory cortex were traced. Fibers of the geniculo-calcarine visual pathways, as well as myocardial fibers running from the epicarduim to the endocardium of the free wall of the left ventricle were tracked. The algorithm was then extended to incorporate prior information of the Frenet characteristics of curvature and torsion into the cost function of the dynamic programming algorithm.

Future goals of this project would include the creation of a database of white

matter and myocardial fibers for brains and hearts in different states. The comparison of density and direction of cortical and myocardial fibers in normal adults and aging adults, as well as in diseased brains and hearts could yield valuable data on how the aging process and various diseases such as stroke and tumor growth in the brain, and arrhythmia, ischemia and ventricular hypertrophy in the heart, affect the fibers. This data could then have high diagnostic value. Other future work could include the application of dynamic programming to the removal of unwanted blood vessels in MR images. The presence of blood vessels in MR images has a significant effect on intensity based white matter segmentation algorithms, and by using dynamic programming to track vessels, it is possible to mask out these unwanted regions from images. Fig. 5.1 shows preliminary work in this area, but there is much need for quantification and validation of the process.

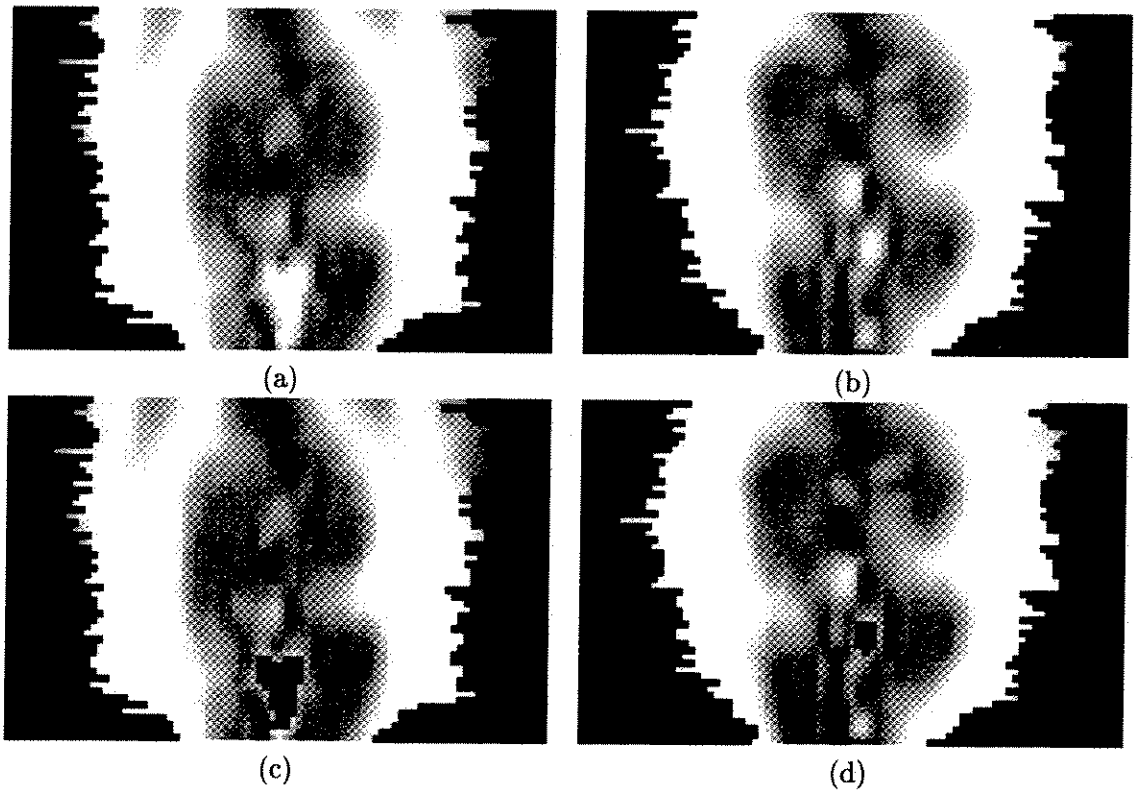

Figure 5.1: Dynamic programming algorithm used to track and mask out unwanted blood vessels. (a)-(b) The MR image with unwanted blood vessel. (c)-(d) The vessel is tracked and masked out through the use of dynamic programming.

Bibliography

[1] D.P. Bertsekas, *Dynamic Programming.* Engleood Cliffs, NJ: Prentice-Hall, Inc. 1987.

[2] D.P. Slichter, *Principles of Magnetic Resonance.* Berlin: Springer-Verlag, 1980.

[3] H.M. Duvernoy, *The Human Brain.* New York: Springer-Verlag Wien, 1991.

[4] D. Haines, *Neuroanatomy: An Atlas of Structures, Sections and Systems.* Baltimore, MD: Urban and Schwarzenberg, 1991.

[5] M.B. Carpenter, *Core Text of Neuroanatomy* Baltimore, MD: William and Wilkins, 1991.

[6] D. Hearn, and M.P. Baker, *Computer Graphics.* Engleood Cliffs, NJ: Prentice-Hall, Inc. 1994.

[7] R.M. Berne, and M.N. Levy, *Cardiovascular Physiology, Seventh Edition.* St. Louis, MI: Mosby-Year Book, Inc. 1997.

[8] S. Russell, and P. Norvig, *Artificial Intelligence, A Modern Approach.* Upper Saddle River, NJ: Prentice-Hall, Inc. 1995.

[9] M.P. Do Carmo, *Differential Geometry of Curves and Surfaces.* Upper Saddle River, NJ: Prentice-Hall, Inc. 1976.

[10] D.B. Cooper, H. Elliott, F. Cohen, L. Reiss, and P. Symosek, "Stochastic Boundary Estimation and Object Recognition," *Image Modeling*, pp. 63–94. New York, NY: Academic Press, 1981

[11] M.A. Fischler, J.M. Tenenbaum, and H.C. Wolf, "Detection of roads and linear structures in low-resolution aerial imagery using a multisource knowledge integration technique," *Computer Graphics and Image Processing*, vol. 15, pp. 210-223, 1981.

[12] U. Grenander, and M. Miller, "Computational Anatomy: An Emerging Discipline," *Quarterly of Applied Mathematics*, vol. 56, pp. 617–694, December, 1998

[13] N. Khaneja, U. Grenander, and M. Miller, "Dynamic programming generation of curves on brain surfaces," *Pattern Analysis and Machine Intelligence*, vol. 20, pp. 1260–1264, November 1998.

[14] N. Khaneja, *Statistics and Geometry of Cortical Features.* St. Louis, MO: M.S. Thesis, Department of Electrical Engineering, Sever Institute of Technology, Washington University, December 1996.

[15] M. Bakircioglu, U. Grenander, N. Khaneja, and M. Miller "Curve Matching on Brain Surfaces using Frenet Distances," *Human Brain Mapping*, vol. 6, pp. 329–333, 1998.

[16] R.R. Petrocelli, J.L. Elion, and K. Manbeck "A New Method for Structure Recognition in Unsubtracted Digital Angiograms," *Proceedings of Computers in Cardiology*, pp. 329–333, October 1992.

[17] R.R. Petrocelli, K. Manbeck, and J.L. Elion "Three Dimensional Structure Recognition in Digital Angiograms Using Gauss-Markov Methods," *Proceedings of Computers in Cardiology*, pp. 329–333, September 1993.

[18] M. Styner, T. Coradi and G. Gerig "Brain Morphometry by Distance Measurement in a non-Euclidean, Curvilinear space," *Proceedings of Information Processing in Medical Imaging*, pp. 364–369, 1999.

[19] Jos Augusto de Azevedo, Joaquim Joo E. R. Silvestre Madeira, Ernesto Q. Vieira Martins, Filipe Manuel A. Pires, "A Shortest Paths Ranking Algorithm", *Proceedings of the Annual Conference AIRO'90 Operational Research Society of Italy*, pp. 1001–1011, 1990.

[20] Ernesto Q. Vieira Martins and Jos Luis E. Santos "A New Shortest Paths Ranking Algorithm", *Investigao Operacional*, vol 20(1), pp. 47-62, 2000.

[21] A. Gueziec, and R. Hummel, "Exploiting Triangulated Surface Extraction using Tetrahedral Decomposition," *IEEE Transactions on Visualization and Computer Graphics*, vol. 1, pp.328–334, 1993.

[22] M. Joshi, *Connected Brain Segmentation and Cortical Surface Generation.* St. Louis,MO.: Master's Thesis, Department of Electrical Engineering, Sever Institute of Technology, Washington University, August 1998.

[23] M. Joshi, J. Cui, K. Doolittle, S. Joshi, D. Van Essen, L. Wang, and M. Miller, "Brain Segmentation and the Generation of Cortical Surfaces," *Neuroimage*, vol. 9, pp. 461–476, 1999.

[24] M. Miller, A. Massie, J. Ratnanather, K. Botteron, and J. Csernansky, "Bayesian Construction of Geometrically based Cortical Thickness Metrics," *Neuroimage*, vol. 12, pp. 676–682, 2000.

[25] S. Ljunggren, "A simple graphical representation of Fourier-based imaging methods," *Journal of Magnetic Resonance*, vol. 54, pp. 338–343, 1983.

[26] S. Mori, and P.B. Barker, "Diffusion Magnetic Resonance Imaging: Its Principle and Applications," *The Anatomical Record (New Anat.)*, vol. 257, pp. 102–109, 1999.

[27] R. Xue, P. van Zijl, B. Crain, M. Solaiyappan, and S. Mori, "In Vivo Three-Dimensional Reconstruction of Rat Brain Axonal Projections by Diffusion Tensor Imaging," *Magnetic Resonance in Medicine*, vol. 42, pp. 1123–1127, 1999.

[28] S. Mori, B. Crain, V.P. Chacko, and P. van Zijl, "Three-Dimensional Tracking of Axonal Projections in the Brain by Magnetic Resonance Imaging," *Annals of Nurology*, vol. 45, pp. 265–269, 1999.

[29] S. Mori, W. Kaufmann, G. Pearlson, B. Crain, B. Stieltjes, M. Solaiyappan, and P. van Zijl, "In Vivo Visulization of Human Neuronal Pathways by Magnetic Resonance Imaging," *Annals of Nurology*, vol. 47, pp. 412–414, March 2000.

[30] T. Conturo, N. Lori, T. Cull, E. Akbudak, A. Snyder, J. Shimony, R. McKinstry, H. Burton, and M. Raichle, "Tracking Neuronal Fiber Pathways in the Living Human Brain," *Proceedings of the National Academy of Science USA*, vol. 96, pp. 10422–10427, March 2000.

[31] C. Poupon, C.A. Clark, V. Frouin, J. Regis, I. Bloch, D. Le Bihan, and J.-F. Mangin, "Regularization of Diffusion-Based Direction Maps for the tracking of Brain White Matter Fasicles," *NeuroImage*, vol. 12, pp. 184–195, 2000.

[32] E.W. Hsu, A.L. Muzikant, S.A. Matulevicius, R.C. Penland, and C.S. Henriquez, "Magnetic resonance myocardial fiber-orientation mapping with direct histological correlation", *American Journal of Physiology: Heart and Circulatory Physiology*, vol. 274, pp 1627–1634, May 1998.

[33] D.F. Scollan, A. Holmes, R. Winslow, and J. Forder, " Histological validation of myocardial microstructure obtained from diffusion tensor magnetic resonance imaging", *American Journal of Physiology: Heart and Circulatory Physiology*, vol. 275, pp H2308–H2318, December 1998.

[34] A. Holmes, D.F. Scollan, R. Winslow, " Direct Histological Validation of Diffusion Tensor MRI in Formaldehyde-Fixed Myocardium", *Magnetic Resonance in Medicine*, vol. 44, pp 157–161, July 2000.

[35] D.H. Laidlaw, E.T. Ahrens, D. Kremers, M.J. Avalos, R.E. Jacobs, and C. Readhead, "Visualizing Diffusion Tensor Images of the Mouse Spinal Cord", *Visualization '98 Conference Proceedings*, pp. 127–134, October 1998

Curriculum Vitæ

Rakesh M. Lal was born in San Fernando, Trinidad and Tobago on April 19, 1978. In 1998, he was accepted into the combined Bachelor/Master of Science in Engineering in Biomedical Engineering at the Johns Hopkins University, Baltimore, Maryland. He graduated with Bachelor of Science in Engineering degrees in Biomedical Engineering and Computer Science from the Johns Hopkins University in May 2001, and he is expected to complete his Master of Science in Engineering degree in Biomedical Engineering by August 2001. His research interests include computational anatomy, differential geometry, image processing and analysis, and scientific computing.